Ionospheric Irregularities During Disturbed Geomagnetic Conditions Over Argentinian EIA Region

Gilda de Lourdes González (gildadelourdes@gmail.com)
Universidad Nacional de Tucumán (UNT) https://orcid.org/0000-0003-4989-3527

Research Article

Keywords: Ionospheric irregularities, Geomagnetic Storms, Equatorial Ionization Anomaly, Scintillation

Posted Date: August 31st, 2021

DOI: https://doi.org/10.21203/rs.3.rs-831490/v1

Version of Record: A version of this preprint was published at Acta Geodaetica et Geophysica on January 20th, 2022. See the published version at https://doi.org/10.1007/s40328-021-00370-4.

Abstract

Ionospheric irregularities can severely degrade radio communication and navigation systems. Geomagnetic storms may affect the generation of these irregularities in a way that is not yet fully understood. To improve the forecasting of this phenomenon, we need to study the ionosphere in different regions of the world, and in particular in the equatorial ionization anomaly (EIA) where irregularities are usually more intense. This study analyses the effect of geomagnetic storms on ionospheric irregularities. We examined the occurrence of irregularities at the southern crest of the EIA in Argentina (Tucumán, 26.9°S, 294.6°E, dip latitude 15.5° S) during three intense and one moderate geomagnetic storm of different solar sources, between 2015 and 2018. We used data from an ionosonde, a Global Positioning System (GPS) receiver and magnetometers. Ionogram spread-F, the F-layer bottom side (h'F), the critical frequency of the F2-layer (foF2), the rate of TEC index (ROTI) and the S4 scintillation index were analysed. The data show irregularities were present as range spread-F and moderate TEC fluctuations in one storm: 27 May 2017 (a coronal mass ejection CME-driven storm occurred on local winter), and were absent in the other events. We suggest that eastward disturbance dynamo electric field and over-shielding prompt penetration electric fields may create favourable conditions for developing these irregularities. Whereas, westward storm time electric fields might inhibit the growth of irregularities during the other storms considered. During co-rotating interaction region CIR-driven storms, the westward disturbance dynamo electric field may be associated with the non-occurrence of irregularities.

1. Introduction

Ionospheric irregularities are regions in the ionosphere with electron density notably different from the background, with scale sizes ranging from tens of centimetres to hundreds of kilometres, and duration between minutes and several hours. These irregularities are a major space weather issue because they can degrade navigational signals, disrupt satellite to ground communications and cause large positioning errors. Ionospheric irregularities depend on local time, season, latitude, longitude, solar, and geomagnetic activity (Abdu, 2012; Madhav Haridas et al., 2018; Tsunoda, 2006). At equatorial and low latitudes, the gravitational Rayleigh-Taylor instability mechanism generates the ionospheric irregularities (Balsley et al., 1972; Dungey, 1956). The major driver for its generation is the vertical ExB drift (Fejer et al., 1999). A seed perturbation, e.g. gravity-waves, is also necessary for the initiation of the irregularities. A variety of techniques have been used to study this phenomenom: radar observations, ground-based Global Navigation Satellite System (GNSS), optical imaging techniques and in situ satellite measurements. Plasma density irregularities of several hundreds of meters can cause rapid fluctuations in the signal amplitude and phase in a received electromagnetic wave, called scintillation. Global Positioning System (GPS) L-band scintillations are caused by irregularities of ~ 400 m scale size. Furthermore, irregularities can manifest as Total Electron Content (TEC) depletions. These are sudden reductions in TEC followed by a recovery to a level near the TEC value preceding the depletion (Valladares et al., 2004). Magdaleno et al. (2012) considered TEC depletions greater than 5 TECu (1 TECu=10^{16} electron/m^2) to be associated with plasma bubbles. In ionograms, irregularities cause backscatter

signatures called spread-F; Range spread-F (RSF) if the broadening is in height and frequency spread-F (FSF) if the broadening is in the frequencies (Piggott & Rawer, 1978). Night-time TEC depletions and scintillations are correlated with ionospheric irregularities at the crest of the equatorial ionization anomaly (EIA) (Dashora & Pandey, 2005). Therefore, GPS derived TEC and amplitude scintillations of L-band frequencies have been used to characterize the irregularities.

The understanding of the short-term and day-to-day variabilities of the ionospheric plasma irregularities is essential to develop predictive capabilities of their occurrence. Different mechanisms drive these short-term variabilities: upward propagating atmospheric waves from the lower atmosphere, or equator-ward propagating disturbances originated during geomagnetic storms. The magnetosphere accumulates energy from the solar wind and dissipates it through geomagnetic storms that drive electrical currents and produce magnetic disturbances. At low latitudes, the ionospheric disturbances during geomagnetically active periods are mainly because of the effects of the prompt penetration electric fields (PPEFs) and the disturbance dynamo electric fields (DDEFs) (Blanc & Richmond, 1980; Senior & Blanc, 1984). Under southward orientation of the interplanetary magnetic field (IMF) Bz and the sudden increase in the AE index, the interplanetary electric field (IEF) is mapped to high latitudes as a dawn-dusk electric field and penetrates nearly instantaneously into low latitudes. This is called prompt penetration/under-shielding electric field and its polarity is eastward (westward) on the day-side (nightside). When Bz turns north and the AE index decreases, the associated over-shielding electric field penetrates to the low latitude ionosphere with opposite polarity of that of the under-shielding electric field (i.e. westward electric fields during the day and eastward at night). The dynamo action of storm time winds driven by the auroral heating process produces the DDEFs. It has a polarity similar to that of the PPEF. It is observed several hours after the storm onset and generates long-lasting perturbations electric fields. The electric field perturbations generated by the PPEF are rapid and short-lived (2–3 h) (Fejer et al., 1979). The thermospheric winds also play a role in the development of irregularities. As it was discussed by Abdu (1997), the global changes in the thermospheric circulation due to the energy deposition at high latitudes during geomagnetic storms cause disturbances in the zonal and meridional winds. At low latitudes, these disturbance winds can modify the vertical plasma drifts and the F-layer height. Changes in the zonal wind can affect the normal development of the PRE (Rishbeth, 1971) and hence, the post-sunset irregularities generation. Whereas, the meridional (or trans-equatorial) wind may affect the field line integrated conductivity and the F layer bottom side gradient, thus inhibiting the irregularities' growth processes (Maruyama, 1988).

Although several studies have been conducted, the effects of geomagnetic storms on ionospheric irregularities are not yet fully understood. Some researchers found that magnetic activity increases the occurrence of irregularities (Fejer et al., 1999). Singh et al. (2015) analysed the equatorial and low-latitude ionosphere response to an intense geomagnetic storm over the Indian sector. They showed that strong scintillation occurred at post-sunset on storm day at low latitudes. They attributed the generation of these irregularities to the enhanced TEC values due to strong evening pre-reversal enhancement in vertical plasma drift/zonal electric field (PRE). Ray et al. (2015) reported that during intense geomagnetic storms,

spread-F generates within four hours of southward Bz crossing -10 nT when under-shielding condition prevails in that longitude sector for which the local time is dusk. Whereas other researchers showed that the occurrence probability of irregularities decreased during geomagnetically active periods (Lyon, Skinner, & Wright, 1960). Sahai et al. (2011) analysed the ionospheric F-region in the Latin American sector during an intense geomagnetic storm and showed that DDEFs inhibited the formation of post-sunset spread-F. Some works concluded that storms trigger post-midnight spread-F (Dabas et al., 1989) and to inhibit the post-sunset ones (Aarons et al., 1980; Alex & Rastogi, 1986). Becker-Guedes et al. (2004) reported that, in the Brazilian sector, post-sunset spread-F was triggered during the low spread-F occurrence season, while it was inhibited during the high spread-F occurrence season. Aarons (1991) proposed that the generation or inhibition of irregularities depends on the local time when maximum Dst decrease occurs due to changes in the normal motions of the F layer. He suggested that if the minimum Dst takes place during daytime hours and before sunset (10-16 LT) then irregularities are inhibited; if minimum Dst occurs in the midnight to post-midnight (0-6 LT) then irregularities are created and if minimum Dst is observed after sunset and before midnight (18-22 LT), the F layer height is not disturbed and the normal pattern of the occurrence of irregularities does not change. Bolaji et al. (2019) pointed out that to study the effects of geomagnetic storms on the occurrence of irregularities, it is necessary to consider the storm timing and the local characteristics. Therefore, studies from different regions are needed to improve our understanding of the short-term behaviour of ionospheric irregularities.

In addition, it is meaningful to take heed of the solar sources of geomagnetic disturbances–coronal mass ejection (CME) or co-rotating interaction region (CIR)–since their characteristics and duration are different (Borovsky & Denton, 2006). Dugassa et al. (2020) pointed out that at equatorial and low-latitudes, the response of ionospheric irregularities to a geomagnetic storm depends on its intensity and driving sources. They found the CME-driven storms led to more enhancement and suppression effects than the CIR-driven storms. They suggested that the difference in the oscillation frequency of IMF Bz in CIR and CME storms may affect the generation of PPEFs and DDEFs and, hence, the development of ionospheric irregularities.

The occurrence characteristics of ionospheric irregularities require more investigation to advance our understanding of the physical mechanisms responsible for its generation and day-to-day variability during disturbed geomagnetic conditions. Hence, improve the forecasting of the occurrence of these irregularities, especially around the EIA where they are most pronounced (Basu et al., 1988). Therefore, we examined the presence of amplitude scintillation, TEC fluctuation and spread-F (RSF and FSF) at a location near the southern crest of the EIA in Argentina (Tucumán, 26.9°S, 294.6°E; magnetic latitude 15.5°S) during two CME-and two CIR-driven geomagnetic storms.

2. Data And Methodology

We used data from a GPS receiver and an ionosonde near the southern crest of the EIA in Argentina (Tucumán, 26.9°S, 294.6°E, dip latitude 15.5° S). The geomagnetic storms considered are listed in table 1, three of them were intense and one was moderate, and they occurred in equinox and winter during the

descending phase of the solar cycle 24. We classified the storms according to the Disturbed Storm Time (Dst) index (Gonzalez et al., 1999): Dst < −100 nT characterized an intense storm and −100 nT ≤ Dst < −50 nT a moderate storm. This index was obtained from the World Data Center (WDC) for Geomagnetism, Kyoto, Japan (http://wdc.kugi.kyoto-u.ac.jp). The value of the monthly mean solar radio flux at 10.7 cm, namely the F10.7 index, is also indicated in table 1 to show the level of solar activity. This index is provided by Dominion Radio Astrophysical Observatory and Natural Resources Canada (https://www.spaceweather.gc.ca/solarflux/sx-en.php). To analyse the geospace condition during the storms, we used the North-South component (Bz) of IMF (obtained from the Advanced Composition Explorer, ACE), the zonal component (Ey) of the IEF, the Kp index (all available at https://omniweb.gsfc.nasa.gov), the AE index (provided by the WDC for Geomagnetism, Kyoto) and the Dst index. When the AE index was not available, we used the SuperMAG electrojet index (SME) (https://supermag.jhuapl.edu/). We got the GPS data from the Low Latitude Ionospheric Sensor Network (LISN) website (http://lisn.igp.gob.pe). A 25° elevation mask was used to reduce the effects of multi-path. We used the scintillation index S4 to quantify the intensity of the amplitude GPS L band scintillation (Davies, 1990). S4 is defined as the normalized standard deviation of the received signal power intensity, I (equation 1) and it is dimensionless. S4 > 0.5 indicates strong scintillation activity and 0.1 < S4 ≤ 0.5 indicates weak scintillation activity.

$$S4 = \sqrt{\frac{\langle I^2\rangle - \langle I\rangle^2}{\langle I\rangle^2}} \qquad (1)$$

The vertical TEC (VTEC) was derived every 10 seconds using the analysis code developed by Seemala and Valladares (2011). To describe the strength of ionospheric irregularities, we used the rate of change of TEC (ROT) (equation 2) and the rate of TEC index (ROTI) (equation 3) along the signal path from each visible satellite to the receiver (Pi et al., 1997).

$$ROT = \frac{TEC_k^i - TEC_{k-1}^i}{t_k - t_{k-1}} \qquad (2)$$

$$ROTI = \sqrt{\langle ROT^2\rangle - \langle ROT\rangle^2} \qquad (3)$$

Where k is the time of epoch and i is the visible satellite. The sampling interval used to calculate ROT is 0.5 min, and the time window of the standard deviation of ROTI is 5 min. ROTI < 0.25 TECU/min indicates no TEC fluctuations, 0.25 ≤ ROTI < 0.5 indicates weak TEC fluctuations, 0.5 ≤ ROTI < 1 moderate TEC fluctuation and ROTI ≥ 1 strong TEC fluctuations (Astafyeva et al., 2018; Ma & Maruyama, 2006). This method detects irregularities with size of ~20 km (Nishioka et al., 2008).

The ionograms were recorded by the Vertical Incidence Pulsed Ionospheric Radar (VIPIR) and are available on the website of the Low Latitude Ionospheric Sensor Network (LISN) (http://lisn.igp.gob.pe). The VIPIR operates between 0.3 and 25 MHz with a sounding repetition of 5 min (Bullett, 2008). Each ionogram was manually examined for the presence of spread-F. We scaled the virtual height of the F-layer bottom side (h'F) and the critical frequency of the F2-layer (foF2). To estimate the quiet-time values of h´F and foF2 we calculated the average for the ten International Quietest Days (IQDs) and the standard deviations (IQDs can be obtained at https://www.gfz-potsdam.de/en/kp-index/).

We used the ΔH parameter to study the occurrence of penetration electric fields. ΔH is the difference in the magnitudes of the horizontal geomagnetic field component (H) between a magnetometer placed on the magnetic equator (Jicamarca, dip latitude 0.4°N) and one displaced 6°-9° away, outside the equatorial electrojet (EEJ) influence (Piura, dip latitude 6.8°N). ΔH is related to the EEJ strength and provide an approximation of the zonal electric field during daytime (De Siqueira Negreti et al., 2017; Yong Wei et al., 2015), this is between 11:00 and 23:00 UT in the Peruvian sector. The magnetometer data can be downloaded from the LISN website.

3. Results

3.1. Storm of 7 October 2015

An intense geomagnetic storm (Dstmin = -124nT, Kp=7) occurred in the early hours of 7 October 2015 (equinox) due to a CIR. This is a boundary zone between slow- and fast-moving solar wind streams. The Dst index showed a two-step response (Figure 1); it decreased to –93 nT at 9 UT (6 LT) then it recovered and decreased again to its minimum value at 22 UT (19 LT). This is a two-phase geomagnetic storm: two main phases and two recovery phases. The highest Kp value was seen at 18 UT (15 LT) on 7 October, AE was highly variable with a peak of 1227 nT at 18 UT (15 LT), a similar irregular behaviour was observed in IMF Bz, it oscillated rapidly between north and south. Whereas Ey (that is proportional to -Vsw x Bz where Vsw is the solar wind speed) also showed oscillations but remained eastward most of the time.

The RSF occurrence rate (number of days with RSF divided by the number of days with data available) during October 2015 was 70%, the FSF occurrence was 20% and the plasma bubble occurrence, detected as TEC depletion greater than 5 TECu (Magdaleno et al., 2012), was 16% (Figure 2). However, no TEC depletions were observed during the period of the storm, and S4 was always below 0.2 (Figure 3). We did not observe spread-F despite h´F is higher than the values for quiet-time between ~0–10 UT (21–7 LT) on 7 October (Figure 4). During the period of the storm, foF2 were close to those of quiet days except on 7 October at 0–6 UT (21–3 LT) when foF2 was lower during disturbed days than during quiet days, this decreased in foF2 is called negative ionospheric storm. There was an irregular behaviour in ΔH (Figure 5) on 7 October between 13-21 UT (10-18 LT). This may be related to the oscillations in IMF Bz, a characteristic of CIR-driven storms. ΔH showed negative values around 17 UT (14 LT) that could be a signature of the presence of a westward electric field.

3.2. Storm of 6 March 2016

A moderate geomagnetic storm occurred on 6 March 2016 (equinox) when a CIR hit the Earth's magnetic field (Figure 6). The minimum Dst (-98 nT) and the maximum Kp index (6) were observed at 21 UT (18 LT). AE showed its highest value (1177 nT) at 17 UT (14 LT), decreased and then increased again to a second peak (770 nT) at 22 UT (19 LT) and it was highly variable during the rest of the day and on the next day. Ey has an irregular behaviour mainly with positive values with peaks of 4.8 mV/m at 18 UT (15 LT), 4.7 mV/m at 16 UT (13 LT) and 4.1 mV/m at 21 UT (18 LT) on 6 March. Bz turned south at ~8 UT (5 LT), and from 16 UT (12 LT) exhibited an oscillatory behaviour between north and south. The oscillations diminished after ~8 UT (5 LT) on 7 March. During each southward turning, the eastward electric field increased.

In March 2016, 48% of the days showed RSF, 30.4% showed FSF (Figure 7) and one day showed strong TEC depletion (not shown here) before the start of the storm: 6 March between 1 and 3 UT (22–0 LT) in coincidence with strong scintillation activity. During the period of the storm, the S4 index was usually lower than 0.2 (Figure 8a) and no TEC fluctuation neither spread-F were observed. As an example, figure 8c shows ROTI values for some satellites on 6 and 7 March. Usually, h´F was close to its quiet-time reference value during the period of the storm (Figure 9), except for 6 March at 19 UT to 7 March at 3 UT and 7 March between 7–11 UT, when storm-time h'F was higher than quiet-time h'F. Finally, foF2 during disturbed days was similar to the quiet values.

ΔH was highly variable during the period of the storm (Figure 10), with negative values on 6 March around 17:30–18:20, 18:30–19:30 and 19:40–20:10 UT (14:30–15:20 LT, 15:30–16:30 LT and 16:40–17:10 LT), this may be related to westward electric fields. Whereas, positive values were observed at 18:20–18:30 UT, 19:30–19:40 and after 20:10 UT. The period 17–21 UT on 6 March corresponds to the main phase of the storm when IMF Bz oscillated from north to south and vice versa and AE showed periods of increase and decrease. This may explain the irregular behaviour observed in ΔH.

3.3. Storm of 27 May 2017

An intense geomagnetic storm occurred on 27 May 2017 (local winter) when an interplanetary CME hit Earth's magnetic field at 15:34 UT (12:34 LT). The minimum Dst (-125nT) was seen on 28 May at 7 UT (4 LT) and the highest Kp (7) occurred at 3 UT (0 LT) (figure 11). Bz presented a strong southward excursion with a peak of -20 nT whereas Ey increased during the storm main phase and reached 7.7 mV/m on 28 May at 0 UT (21 LT). AE showed three peaks, 1270 nT at ~5 UT (2 LT), 1163 nT at ~2 UT (23 LT) on 28 May and 949 nT at 23 UT (20 LT) on 27 May. A second enhancement of the geomagnetic activity occurred on 29 May at ~13 UT (10 LT): Bz reached -12 nT, Ey = 4.5 mV/m, Kp = 4 and one hour later AE was 839 nT.

During the period of the storm, we observed weak L band scintillation activity (Figure 12a). TEC depletions were seen during the main phase of the storm, on 28 May around 1–5:30 UT (22–2:30 LT) (Figure 12c) but TEC depletion greater than 5 TECu were only present in one day of the month: May 4 (not shown here). According to the ROTI values, moderate and weak TEC fluctuations were present during the main phase of the storm. Figure 12d depicts some examples for PRN 13, 15, 17 and 24. The RSF

occurrence rate was 64.5% in May 2017 and, during the main phase of the storm RSF, was present for several hours: on May 28 from 00:43 to 7:33 UT (27 May, 21:43–28 May, 4:33 LT). Figure 12b shows an example of an ionogram with RSF recorded on 28 May, and figure 13 depicts the RSF and FSF occurrence during the entire month. An increased in h´F was seen in 28 May at 0–2 UT (Figure 14), when it was higher that the quiet-time levels. We could not get the height values on 28 May between 3–10 UT because of the presence of spread-F in the ionograms. During 27 and 29 May, storm-time h´F was similar to the quiet-time h´F. The foF2 was usually close to the quiet-time levels, except on 28 March at ~14–20 UT, when a positive ionospheric storm (increase in foF2) was observed. ΔH showed positive values during the period of the storm considered, whereas it was negative on 29 May at ~11:30–14 UT (8:30–11 LT) when a substorm was observed, negative values in ΔH may be the effect of westward electric fields (Figure 15).

3.4. Storm of 25 August 2018

On 25 August 2018 (local winter), an interplanetary CME hit the Earth's magnetic field and triggered an intense geomagnetic storm. The source of this CME was probably a filament eruption observed on 20 August (Piersanti et al., 2020). The Dst reached a minimum value of -174nT and Kp a maximum of 7 at ~7 UT (4 LT) on 26 August (Figure 16). Bz flipped southward on 25 August at ~16 UT (13 LT) and showed an oscillatory behaviour on 26 August at 8–20 UT (5–17 LT). Ey increased from 25 August at 14 UT (11 LT) and peaked at 5 UT (2 LT), like Bz, Ey also presented an irregular behaviour after 8 UT on 26 August, with mostly positive values. There were no data available for the AE index during the period of the storm, so we decided to use the SME index to evaluate the auroral zone magnetic activity. SME increased from 25 August at around 17 UT (14 LT) and its highest value was 1565 nT at ~3 UT (~0 LT) on 26 August. Then, it irregularly decreased to quiet values and increased again after 0 UT on 27 August (22 LT on 26 August).

During the period of the storm, S4 was usually lower than 0.2 and ROTI was lower than 0.5, this means weak L band scintillation and weak TEC fluctuation were present. Figure 17 depicts the S4 index and, as an example, the ROTI for PRN 26 during 25-27 August 2018. There were no ionosonde data for most of August 2018, so we did not calculate the spread-F occurrence rate for this month, however previous researchers have found that in winter months during low solar activity–such as August 2018–spread-F occurrence is high at the southern crest of the EIA (Candido et al., 2011). But, during the days of the storm, the ionograms did not show spread-F. The disturbed h´F values were usually similar to the quiet-time values (Figure 18) but on 26 August at ~20 UT (~17 LT) h'F was higher during the storm than during quiet days. Whereas, a positive ionospheric storm was observed on 26 August at 0–6 UT (21–3 LT), at 12–18 UT (9–15 LT) and on 27 August at 12–19 UT (9–16 LT). ΔH (Figure 19) was negative on 26 August at 11–15 UT (8–12 LT) and 15:30–18:30 UT (12:30–15:30 LT), during part of the main phase and the recovery phase of the storm. Then, ΔH turned positive on 26 August at ~19–23 UT (~16–20 LT), during the recovery phase.

4. Discussion

Only one of the four geomagnetic storms showed ionospheric irregularities: 27 May 2017. This was an intense storm driven by a CME. It occurred in local winter during low solar activity (mean F10.7=75.2 sfu). RSF, moderate TEC fluctuation and weak GPS L band scintillation were seen during the storm's main phase. The RSF started at ~22 LT on 27 May and lasted until ~ 4 LT on 28 May. Whereas, the TEC fluctuation vanished around 2 LT. During this period, Bz was turning north, Ey was decreasing and AE was increasing irregularly. These irregularities may be related to an eastward DDEF that might be acting since the irregularities were seen several hours after the storm onset. Another possibility is the effect of an over-shielding eastward electric field that reached low latitudes, associated with the Bz turning north at this time. ΔH is used to assess the occurrence of penetration electric fields during the daytime, due to higher Cowling conductivity during the day than at night. However, several researchers reported PPEF signatures in ΔH on the nightside (Fejer et al., 2007; Galav et al., 2011). Moreover, Wei et al. (2013) concluded that nightside ΔH can sometimes manifest a PPEF in the midnight-dawn sector (00–05 LT). We observed that on 28 May, ΔH increased between 2–8 UT (23–5 LT), this may be associated with an eastward penetration electric field.

During this storm, we observed RSF, but the amplitude scintillation was weak. The ionospheric irregularities detected by the ionosonde and the GPS receiver are of different sizes; the amplitude scintillation is caused by irregularities of few hundreds of meters of scale-size whereas, the ionosonde can detect larger-scale irregularities (>1 km) (E. R. de Paula et al., 2007 and references therein). Therefore, the irregularities present on this day may be larger than those necessary for scintillation to occur.

Our observations for the May storm suggest eastward storm time electric fields (PPEF and/or DDEF) may induce disturbance upward ExB drifts that rise the F region to heights of lower ion-neutral collision frequency and lower recombination rate. An increase in the h´F values was observed during the main phase of the storm. This could enhance the growth rate of the gravitational Rayleigh-Taylor instability mechanism and help create favourable conditions for irregularities to develop (if a seed perturbation is present). The results are consistent with the studies carried out by Abdu et al. (2012). They concluded that post-midnight spread F can develop from over-shielding electric fields during two moderate geomagnetic storms at low latitudes in Brazil. Also in Brazil, Sahai et al. (2007) reported plasma bubbles during the recovery phase of an intense geomagnetic storm in winter. For the other storms under consideration, the prompt penetration of electric fields and/or the disturbance dynamo electric field of westward polarity may cause a downward drift of the F-region plasma and might inhibit the formation of irregularities. Possible signatures of these westward electric fields can be observed in ΔH during the March and the August storms. At low latitudes in Brazil, de Paula et al. (2019) reported that ionogram spread-F, GPS and VHF amplitude scintillations were completely inhibited during a geomagnetic storm in September 2017. They suggested westward DDEFs caused a strong counter-electrojet (negative ΔH values) and a downward movement of the F layer height, and therefore suppressed the formation of irregularities. de Abreu et al. (2017) showed that over the American sector, ionospheric irregularities were not affected by the intense geomagnetic storm on 1–3 June 2013. Dugassa et al. (2020) reported that during the solar minimum period 2007 to 2009, there were no significant effects of geomagnetic storms in the occurrence of ionospheric irregularities over low-latitudes in Africa. Previous studies observed

similar behaviour in different longitudes e.g. Abdu et al. (2006), Amaechi et al. (2018), Ngwira et al. (2013). In the present work, we may attribute the absence of ionospheric irregularities in three of the four storms examined to the effect of westward DDEFs and/or westward PPEFs. An over-shielding (under-shielding) electric field associated with the northward (southward) orientation of Bz acting during post-sunset (post-midnight) hours may suppress the generation of ionospheric irregularities at the southern crest of the EIA. Irregularities usually occur after large and consistent southward excursions in Bz during post-sunset (Martinis et al., 2005), for the CIR-driven storms (October and March storms) and during the recovery phase of the August storm, the oscillatory behaviour—several short-lived southward and northward turnings—in Bz may create several under-shielding and over-shielding electric fields with opposite polarity. Therefore, the effect of the penetration electric fields may not be significant and the DDEF could be the main cause of the inhibition of irregularities. However, other parameters might affect the development of irregularities during disturbed periods at low latitudes, e.g. gravity waves or travelling ionospheric disturbances due to storm time Joule heating in the auroral zone.

The minimum Dst during the May storm occurred in the post-midnight period and, according to Aarons (1991) the F layer height should rise and create irregularities. Our observations agree with this hypothesis. However, the August storm also presented the minimum Dst at post-midnight, but we did not detect irregularities. During the October and March storms, the minimum Dst took place after sunset, Aarons (1991) suggests the storm has no significant effect and irregularities may form as on a quiet night, nevertheless, we did not see post-sunset irregularities that were present in several quiet days in October and March. Shang et al. (2008) analysed the effect of strong geomagnetic storms on L-band ionospheric scintillation over the eastern Asia equatorial region, they showed that for CME-driven storms, when the maximum negative excursion of Dst occurs after 03 LT to the early morning hours, no scintillation was observed in the latter half of the night. Our results for the May storm and for the August storm (both driven by CMEs) agree with this conclusion. For these events, the minimum Dst took place at 4 and 3 LT respectively, and we did not see irregularities during the rest of the night. For the May storm, spread-F vanished at ~ 4 LT, whereas for the August storm, no irregularities were detected.

On 6 October at 21–7 LT and on 7 March at 4–8 LT the F-layer rose to higher values than during quiet time, but irregularities were not detected, this may imply that other processes could inhibit the development of the irregularities at this time. At low latitudes, changes in the F-layer height can be caused by the disturbance thermospheric meridional winds generated in the auroral zone that travel to the equatorial region (Sahai et al., 2011), F-layer height increases in the upwind hemisphere whereas it decreases in the downwind hemisphere. Shang et al. (2008) suggested that the disturbance of neutral winds might be responsible for the suppression of scintillation. This conforms to previous researchers (Maruyama, 1988; Abdu, 1997) who pointed out that the meridional disturbance winds that control the flux tube-integrated conductivity and the F layer bottom side gradient may inhibit or slow down the development of ionospheric irregularities by modifying its growth rate. Also, trans-equatorial winds can create a latitudinal asymmetry in the EIA that may retard or suppress the development of the irregularities. It seems reasonable to suggest that the trans-equatorial/meridional winds might be one reason for the absence of irregularities during these periods.

In Tucumán, during the descending phase of solar cycle 24, the low spread-F occurrence season was equinox and the high spread-F season was summer except in 2018 when the highest spread-F occurrence was winter (González, 2021). In this study, spread-F was absent during the storms of October 2015, March 2016 (equinox) and August 2018 (local winter), whereas it was present during the May 2017 storm (local winter). Becker-Guedes et al. (2004) showed that, in the Brazilian sector, geomagnetic storms trigger post-sunset spread-F during the low spread-F occurrence season and inhibit it during the high spread-F occurrence season. Our observations partially agree with this statement: irregularities did not develop during a storm occurred in a month of high occurrence rate of spread-F (August 2018, local winter) over Tucumán.

5. Conclusions

We examined the occurrence of ionospheric irregularities during four geomagnetic storms at a station near the southern crest of the EIA in South America (Tucumán, 26.9°S, 294.6°E, dip latitude 15.5° S).

The main outcomes of this study are:

1. RSF, moderate TEC fluctuation and weak GPS L band scintillation were seen during the main phase of the May storm, an intense storm driven by a CME. The irregularities onset was ~22 LT and lasted until post-midnight. We suggest that eastward DDEF and over-shielding electric fields may be responsible for the generation of these irregularities.

2. Ionospheric irregularities were absent during the other three storms analysed. A possibility is that westward PPEFs and DDEFs may inhibit the growth of the irregularities.

3. Other factors, e.g., disturbance winds, might also affect the generation of irregularities during the considered storms. This needs to be further analysed.

Declarations

Funding The present study was supported by Universidad del Norte Santo Tomás de Aquino.

Conflicts of interest/Competing interests The author declares that she has no competing interest.

Availability of data and material The ionosonde and GPS data are available at http://lisn.igp.gob.pe/

Code availability Not applicable

Acknowledgement

Thanks to the following groups for making data publicly available: the Low Latitude Ionospheric Sensor Network (LISN); the UMass Lowell Center for Atmospheric Research; the NASA/Goddard's Space Physics

Data Facility; the International Service of Geomagnetic Indices; the GFZ German Research Center for Geosciences at Potsdam and the World Data Center (WDC) Kyoto, Japan.

References

1. Aarons, J., Mullen, J. P., Koster, J. P., DaSilva, R. F., Medeiros, J. R., Medeiros, R. T., … Paulson, M. R. (1980). Seasonal and geomagnetic control of equatorial scintillations in two longitudinal sectors. *Journal of Atmospheric and Terrestrial Physics*, *42*(9–10), 861–866.
2. Aarons, J. (1991). The role of the ring current in the generation or inhibition of equatorial F layer irregularities during magnetic storms. *Radio Science*, *26*(4), 1131–1149. https://doi.org/10.1029/91RS00473
3. Abdu, M. A. (1997). Major phenomena of the equatorial ionosphere-thermosphere system under disturbed conditions. *Journal of Atmospheric and Solar-Terrestrial Physics*, *59*(13), 1505–1519. Retrieved from https://doi.org/10.1016/S1364-6826(96)00152-6
4. Abdu, M. A. (2012). Equatorial spread F/plasma bubble irregularities under storm time disturbance electric fields. *Journal of Atmospheric and Solar-Terrestrial Physics*, *75–76*, 44–56. https://doi.org/10.1016/j.jastp.2011.04.024
5. Abdu, M. A., Batista, I. S., Bertoni, F., Reinisch, B. W., Kherani, E. A., & Sobral, J. H. A. (2012). Equatorial ionosphere responses to two magnetic storms of moderate intensity from conjugate point observations in Brazil. *Journal of Geophysical Research: Space Physics*, *117*(5), 1–20. https://doi.org/10.1029/2011JA017174
6. Alex, S., & Rastogi, R. G. (1986). Geomagnetic disturbance effect on equatorial spread-F. *Annales Geophysicae*, *2*(2), 82–88. Retrieved from https://www.prl.res.in/~library/rg_rastogi_5_2_83_1987.pdf
7. Astafyeva, E., Zakharenkova, I., Hozumi, K., Alken, P., Coïsson, P., Hairston, M. R., & Coley, W. R. (2018). Study of the Equatorial and Low-Latitude Electrodynamic and Ionospheric Disturbances During the 22–23 June 2015 Geomagnetic Storm Using Ground-Based and Spaceborne Techniques. Journal of Geophysical Research: Space Physics, 123(3), 2424–2440. https://doi.org/10.1002/2017JA024981
8. Balsley, B. B., Haerendel, G., & Greenwald, R. A. (1972). Equatorial spread F : Recent observations and a new interpretation. *Journal of Geophysical Research*, *77*(28), 5625–5628. https://doi.org/10.1029/JA077i028p05625
9. Basu, S., MacKenzie, E., & Basu, S. (1988). Ionospheric constraints on VHF/UHF communications links during solar maximum and minimum periods. *Radio Science*, *23*(3), 363–378. https://doi.org/10.1029/RS023i003p00363
10. Blanc, M., & Richmond, A. D. (1980). The Ionospheric Dynamo. *Journal of Geophysical Research*, *85*(9), 1669–1686.https://doi.org/10.1029/JA085iA04p01669
11. Becker-Guedes, F., Sahai, Y., Fagundes, P. R., Lima, W. L. C., Pillat, V. G., Abalde, J. R., & Bittencourt, J. A. (2004). Geomagnetic storm and equatorial spread-F. *Annales Geophysicae*, *22*(9), 3231–

3239.https://doi.org/10.5194/angeo-22-3231-2004

12. Bolaji, O. S., Adebiyi, S. J., & Fashae, J. B. (2019). Characterization of ionospheric irregularities at different longitudes during quiet and disturbed geomagnetic conditions. *Journal of Atmospheric and Solar-Terrestrial Physics*, *182*, 93–100. https://doi.org/10.1016/j.jastp.2018.11.007
13. Borovsky, J. E., & Denton, M. H. (2006). Differences between CME-driven storms and CIR-driven storms. *Journal of Geophysical Research*, *111*(A7), A07S08. https://doi.org/10.1029/2005JA011447
14. Bullett, T. (2008). *Station Report : A new ionosonde at Boulder* (Issue November). https://www.sws.bom.gov.au/IPSHosted/INAG/web-69/2008/boulder_vipir.pdf
15. Candido, C. M. N., Batista, I. S., Becker-Guedes, F., Abdu, M. A., Sobral, J. H. A., & Takahashi, H. (2011). Spread F occurrence over a southern anomaly crest location in Brazil during June solstice of solar minimum activity. *Journal of Geophysical Research: Space Physics*, *116*(6), 2008–2009. https://doi.org/10.1029/2010JA016374
16. Dabas, R. S., Lakshmi, D. R., & Reddy, B. M. (1989). Effect of geomagnetic disturbances on the VHF nighttime scintillation activity at equatorial and low latitudes. *Radio Science*, *24*(4), 563–573. https://doi.org/10.1029/RS024i004p00563
17. Dashora, N., & Pandey, R. (2005). Observations in equatorial anomaly region of total electron content enhancements and depletions. *Annales Geophysicae*, *23*(7), 2449–2456. https://doi.org/10.5194/angeo-23-2449-2005
18. Davies, K. (1990). Ionospheric Radio. Ionospheric Radio. https://doi.org/10.1049/pbew031e Gonzalez, W. D., Tsurutani, B. T., & Clúa De Gonzalez, A. L. (1999). Interplanetary origin of geomagnetic storms. Space Science Reviews, 88(3–4), 529–562. https://doi.org/10.1023/a:1005160129098
19. de Abreu, A. J., Martin, I. M., Fagundes, P. R., Venkatesh, K., Batista, I. S., de Jesus, R., … Wild, M. (2017). Ionospheric F-region observations over American sector during an intense space weather event using multi-instruments. *Journal of Atmospheric and Solar-Terrestrial Physics*, *156*, 1–14. https://doi.org/10.1016/j.jastp.2017.02.009
20. de Paula, E. R., Kherani, E. A., Abdu, M. A., Batista, I. S., Sobral, J. H. A., Kantor, I. J., Takahashi, H., de Rezende, L. F. C., Muella, M. T. A. H., Rodrigues, F. S., Kintner, P. M., Ledvina, B. M., Mitchell, C., & Groves, K. M. (2007). Characteristics of the ionospheric F-region plasma irregularities over brazilian longitudinal sector. *Indian Journal of Radio and Space Physics*, *36*(4), 268–277.
21. de Paula, E. R., de Oliveira, C. B. A., Caton, R. G., Negreti, P. M., Batista, I. S., Martinon, A. R. F., … Moraes, A. O. (2019). Ionospheric irregularity behavior during the September 6–10, 2017 magnetic storm over Brazilian equatorial–low latitudes. *Earth, Planets and Space*, *71*(1). https://doi.org/10.1186/s40623-019-1020-z
22. De Siqueira Negreti, P. M., De Paula, E. R., & Maria Nicoli Candido, C. (2017). Total electron content responses to HILDCAAs and geomagnetic storms over South America. *Annales Geophysicae*, *35*(6), 1309–1326. https://doi.org/10.5194/angeo-35-1309-2017

23. Dugassa, T., Habarulema, J. B., & Nigussie, M. (2020). Statistical study of geomagnetic storm effects on the occurrence of ionospheric irregularities over equatorial/low-latitude region of Africa from 2001 to 2017. *Journal of Atmospheric and Solar-Terrestrial Physics*, *199*, 105198. https://doi.org/10.1016/j.jastp.2020.105198
24. Dungey, J. W. (1956). Convective diffusion in the equatorial F region. *Journal of Atmospheric and Terrestrial Physics*, *9*(5–6), 304–310. https://doi.org/10.1016/0021-9169(56)90148-9
25. Fejer, B. G., Gonzales, C. A., Farley, D. T., Kelley, M. C., & Woodman, R. F. (1979). Equatorial Electric Fields During Magnetically Disturbed Conditions - 1. the Effect of the Interplanetary Magnetic Field. *Journal of Geophysical Research*, *84*(A10), 5797–5802. https://doi.org/10.1029/JA084iA10p05797
26. Fejer, B. G., Scherliess, L., & de Paula, E. R. (1999). Effects of the vertical plasma drift velocity on the generation and evolution of equatorial spread F. *Journal of Geophysical Research: Space Physics*, *104*(A9), 19859–19869. https://doi.org/10.1029/1999JA900271
27. Fejer, B. G., Jensen, J. W., Kikuchi, T., Abdu, M. A., & Chau, J. L. (2007). Equatorial Ionospheric Electric Fields During the November 2004 Magnetic Storm. *Journal of Geophysical Research: Space Physics*, *112*(A10), n/a-n/a. https://doi.org/10.1029/2007JA012376
28. Galav, P., Sharma, S., & Pandey, R. (2011). Study of simultaneous penetration of electric fields and variation of total electron content in the day and night sectors during the geomagnetic storm of 23 May 2002. *Journal of Geophysical Research: Space Physics*, *116*(12), 1–10. https://doi.org/10.1029/2011JA017002
29. González, G. de L. Spread-F characteristics at the southern anomaly crest in South America during the descending phase of solar cycle 24, 22 April 2021, PREPRINT (Version 1) available at Research Square https://doi.org/10.21203/rs.3.rs-452354/v1
30. Lyon, A. J., Skinner, N. J., & Wright, R. W. H. (1960). The belt of equatorial spread-F. *Journal of Atmospheric and Terrestrial Physics*, *19*(3–4), 145–159. https://doi.org/10.1016/0021-9169(60)90043-X
31. Ma, G., & Maruyama, T. (2006). A super bubble detected by dense GPS network at east Asian longitudes. Geophysical Research Letters, 33(21), 1–5. https://doi.org/10.1029/2006GL027512
32. Madhav Haridas, M. K., Manju, G., & Arunamani, T. (2018). Solar activity variations of equatorial spread F occurrence and sustenance during different seasons over Indian longitudes: Empirical model and causative mechanisms. *Advances in Space Research*, *61*(10), 2585–2592. https://doi.org/10.1016/j.asr.2018.02.040
33. Magdaleno, S., Herraiz, M., & de la Morena, B. A. (2012). Characterization of equatorial plasma depletions detected from derived GPS data in South America. *Journal of Atmospheric and Solar-Terrestrial Physics*, *74*, 136–144. https://doi.org/10.1016/j.jastp.2011.10.014
34. Martinis, C. R., Mendillo, M. J., & Aarons, J. (2005). Toward a synthesis of equatorial spread F onset and suppression during geomagnetic storms. *Journal of Geophysical Research: Space Physics*, *110*(A7), 1–12. https://doi.org/10.1029/2003JA010362

35. Maruyama, T. (1988). A diagnostic model for equatorial spread F , 1, Model description and application to electric field and neutral wind effects. *Journal of Geophysical Research*, *93*(A12), 14611. https://doi.org/10.1029/JA093iA12p14611
36. Nishioka, M., Saito, A., & Tsugawa, T. (2008). Occurrence characteristics of plasma bubble derived from global ground-based GPS receiver networks. *Journal of Geophysical Research: Space Physics*, *113*(5), 1–12. https://doi.org/10.1029/2007JA012605
37. Pi, X., Mannucci, A. J., Lindqwister, U. J., & Ho, C. M. (1997). Monitoring of global ionospheric irregularities using the worldwide GPS network. *Geophysical Research Letters*, *24*(18), 2283–2286. https://doi.org/10.1029/97GL02273
38. Piersanti, M., De Michelis, P., Del Moro, D., Tozzi, R., Pezzopane, M., Consolini, G., … Diego, P. (2020). From the Sun to Earth: effects of the 25 August 2018 geomagnetic storm. *Annales Geophysicae*, *38*(3), 703–724. https://doi.org/10.5194/angeo-38-703-2020
39. Piggott, W. R., & Rawer, K. (1978). *Revision of Chapters 1-4 U.R.S.I. Handbook of Ionogram Interpretation and Reduction. Report UAG-23A*. Boulder, Colorado: World Data Center A for Solar-Terrestrial Physics, NOAA. Retrieved from https://www.sws.bom.gov.au/IPSHosted/INAG/uag_23a/uag_23a.html
40. Ray, S., Roy, B., & Das, A. (2015). Occurrence of equatorial spread F during intense geomagnetic storms. *Radio Science*, *50*(7), 563–573. https://doi.org/10.1002/2014RS005422
41. Rishbeth, H. (1971). Polarization fields produced by winds in the equatorial F-region. *Planetary and Space Science*, *19*(3), 357–369. https://doi.org/10.1016/0032-0633(71)90098-5
42. Sahai, Y., Becker-Guedes, F., Fagundes, P. R., Lima, W. L. C., Otsuka, Y., Huang, C. S., … Bittencourt, J. A. (2007). Response of nighttime equatorial and low latitude F-region to the geomagnetic storm of August 18, 2003, in the Brazilian sector. *Advances in Space Research*, *39*(8), 1325–1334. https://doi.org/10.1016/j.asr.2007.02.064
43. Sahai, Y., Fagundes, P. R., de Jesus, R., de Abreu, A. J., Crowley, G., Kikuchi, T., … Bittencourt, J. A. (2011). Studies of ionospheric F-region response in the Latin American sector during the geomagnetic storm of 21–22 January 2005. *Annales Geophysicae*, *29*(5), 919–929. https://doi.org/10.5194/angeo-29-919-2011
44. Seemala, G. K., & Valladares, C. E. (2011). Statistics of total electron content depletions observed over the South American continent for the year 2008. Radio Science, 46(5), 1–14. https://doi.org/10.1029/2011RS004722
45. Senior, C., & Blanc, M. (1984). On the Control of Magnetospheric Convection by the Spatial Distribution of Ionospheric Conductivities. *Journal of Geophysical Research*, *89*(A1), 261–284. https://doi.org/10.1029/JA089iA01p00261
46. Shang, S. P., Shi, J. K., Kintner, P. M., Zhen, W. M., Luo, X. G., Wu, S. Z., & Wang, G. J. (2008). Response of Hainan GPS ionospheric scintillations to the different strong magnetic storm conditions. *Advances in Space Research*, *41*(4), 579–586. https://doi.org/10.1016/j.asr.2007.05.020

47. Singh, R., Sripathi, S., Sreekumar, S., Banola, S., Emperumal, K., Tiwari, P., & Kumar, B. S. (2015). Low-latitude ionosphere response to super geomagnetic storm of 17/18 March 2015: Results from a chain of ground-based observations over Indian sector. *Journal of Geophysical Research: Space Physics*, *120*(12), 10,864-10,882. https://doi.org/10.1002/2015JA021509
48. Tsunoda, R. T. (2006). Day-to-day variability in equatorial spread F: Is there some physics missing? *Geophysical Research Letters*, *33*(16). https://doi.org/10.1029/2006GL025956
49. Valladares, C. E., Villalobos, J., Sheehan, R., & Hagan, M. P. (2004). Latitudinal extension of low-latitude scintillations measured with a network of GPS receivers. *Annales Geophysicae*, *22*(9), 3155–3175. https://doi.org/10.5194/angeo-22-3155-2004
50. Wei, Y., Fraenz, M., Dubinin, E., He, M., Ren, Z., Zhao, B., … Alex, S. (2013). Can a nightside geomagnetic Delta H observed at the equator manifest a penetration electric field? *Journal of Geophysical Research: Space Physics*, *118*(6), 3557–3567. https://doi.org/10.1002/jgra.50174
51. Wei, Y., Zhao, B., Li, G., & Wan, W. (2015). Electric field penetration into Earth's ionosphere: a brief review for 2000–2013. *Science Bulletin*, *60*(8), 748–761. https://doi.org/10.1007/s11434-015-0749-4

Tables

Table 1. Geomagnetic storms analysed in this work, their minimum Dst value, the type of storm according to the Dst index (weak, moderate or intense), the monthly mean F10.7 (in solar flux units, sfu) and the season of occurrence.

Storm day	Minimum Dst (nT)	Type of storm	Monthly mean F10.7 (sfu)	Season
7/10/2015	-124	Intense	103.3	equinox
6/3/2016	-98	moderate	90.6	equinox
27/5/2017	-125	intense	75.2	winter
25/8/2018	-174	intense	70.8	winter

Figures

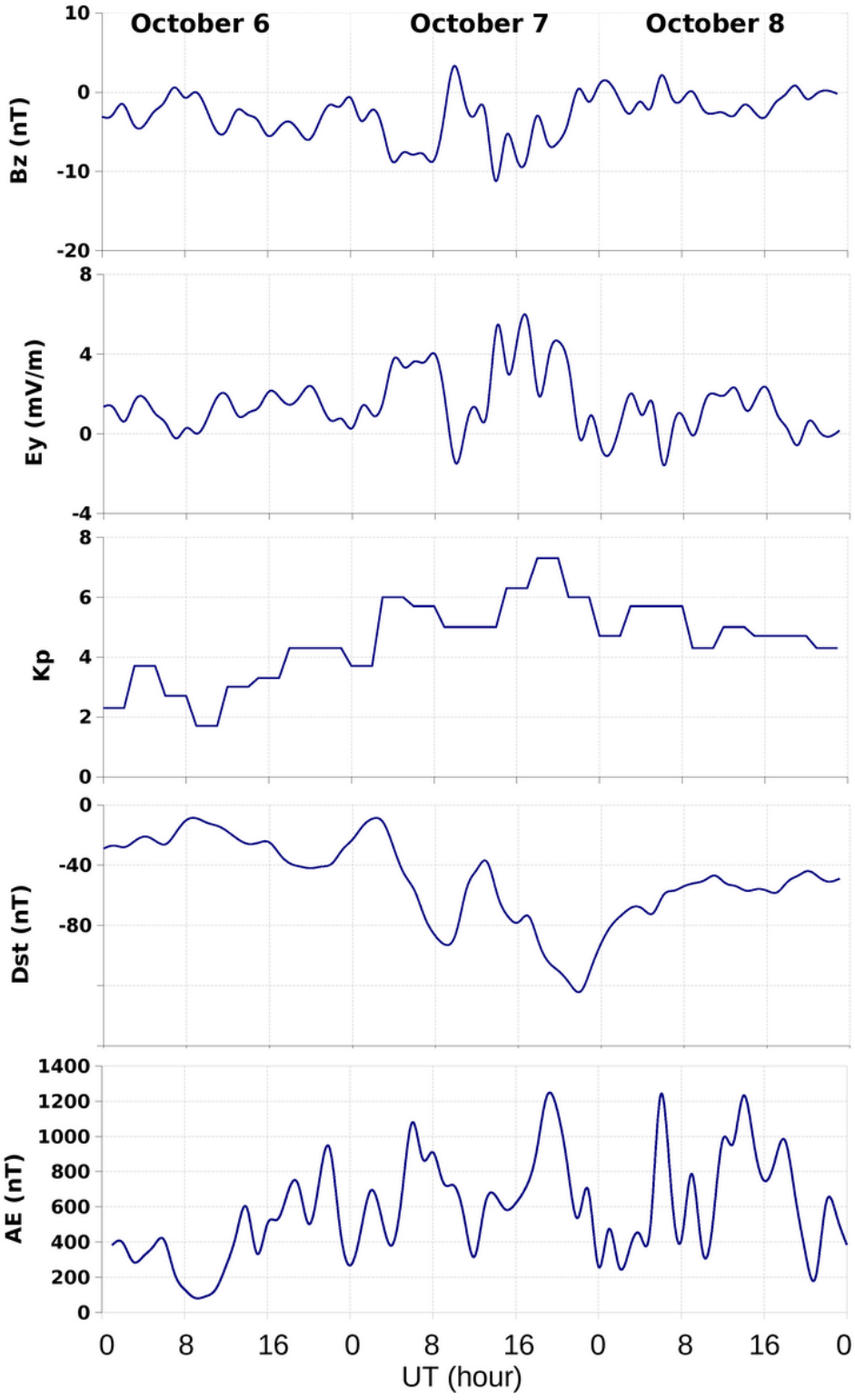

Figure 1

Bz, Ey, Kp, Dst and AE during 6-8 October 2015

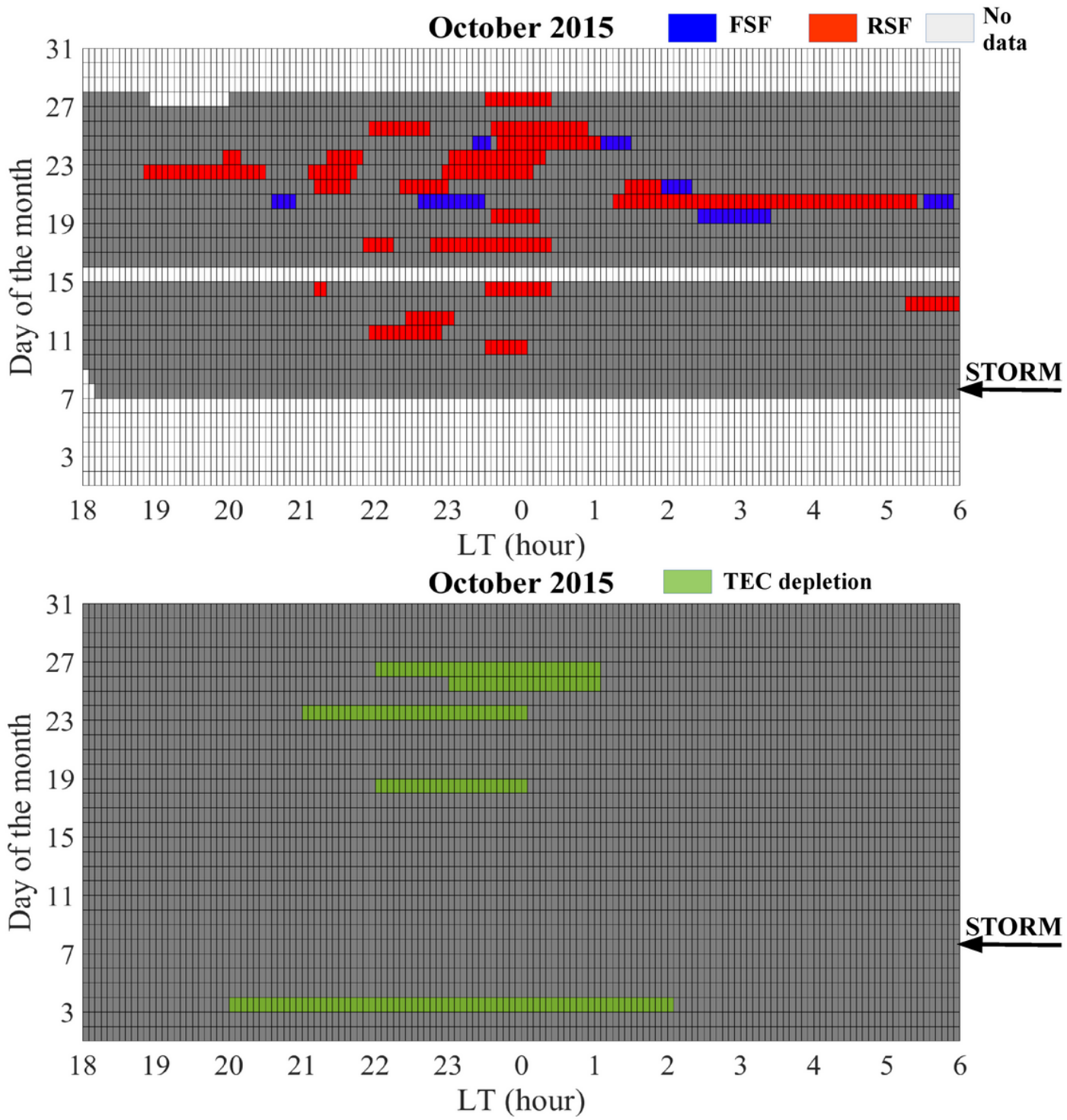

Figure 2

Top panel, range spread-F (RSF) occurrence (red) and frequency spread-F (FSF) occurrence (blue) at Tucumán during October 2015. White indicates data gaps. Bottom panel, strong TEC depletions occurrence (green) during October 2015

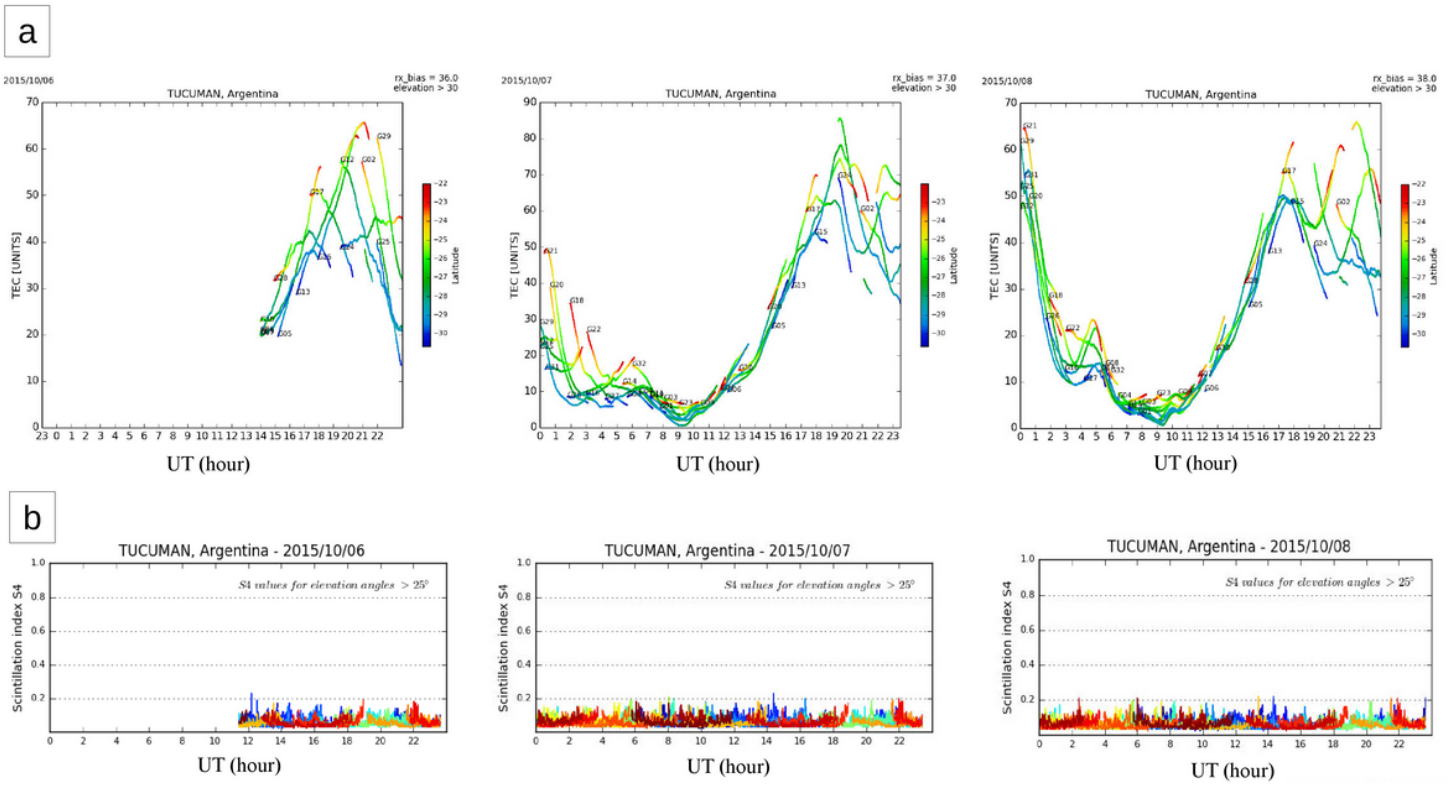

Figure 3

a) TEC for different satellites at Tucumán on 6, 7 and 8 October 2015. b) S4 index for different satellites on 6, 7 and 8 October 2015. Different colours indicate different satellites

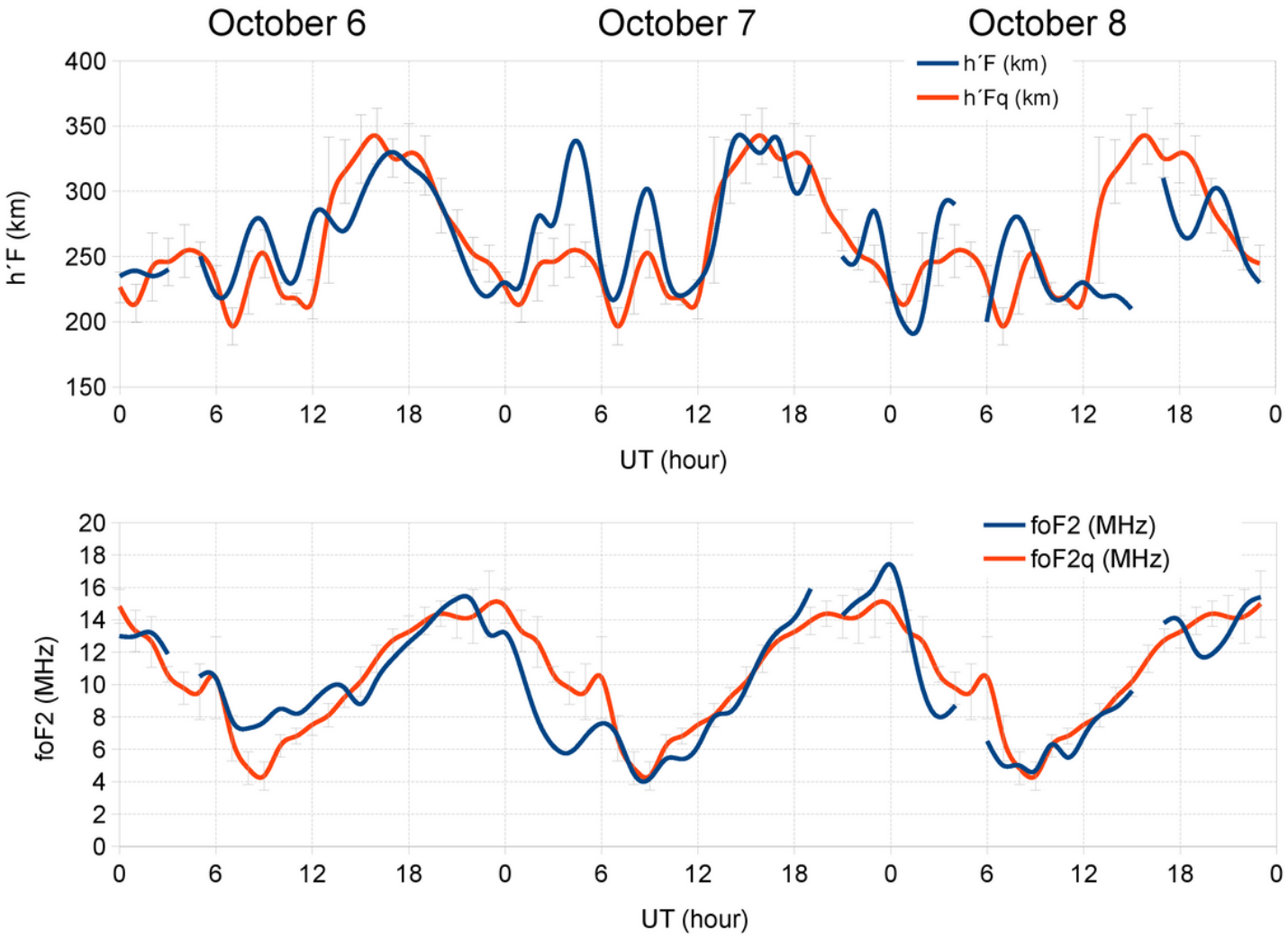

Figure 4

h´F and foF2 at Tucumán during 6-8 October 2015. The grey lines are ±1 standard deviation of the average quiet day's value

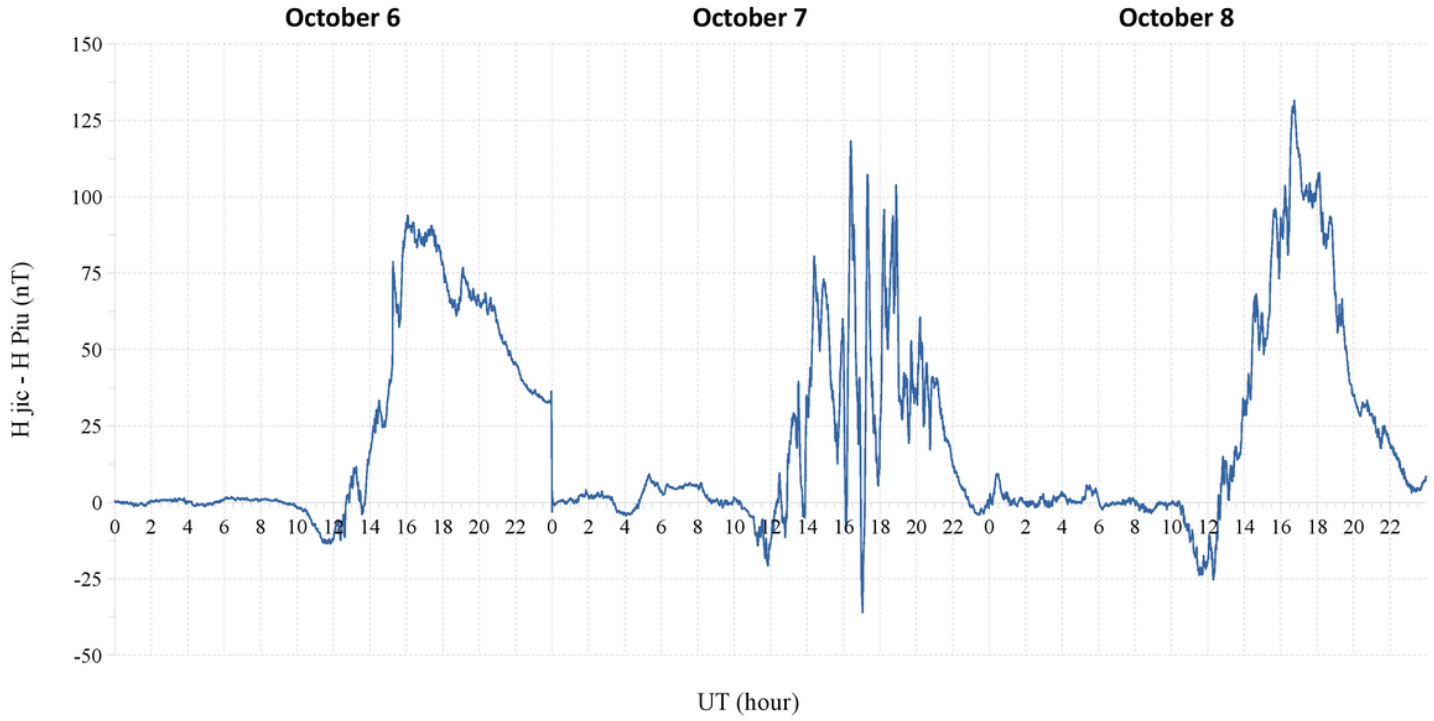

Figure 5

Difference between horizontal geomagnetic field components (H) at Jicamarca and Piura, Peru, during 6-8 October 2015

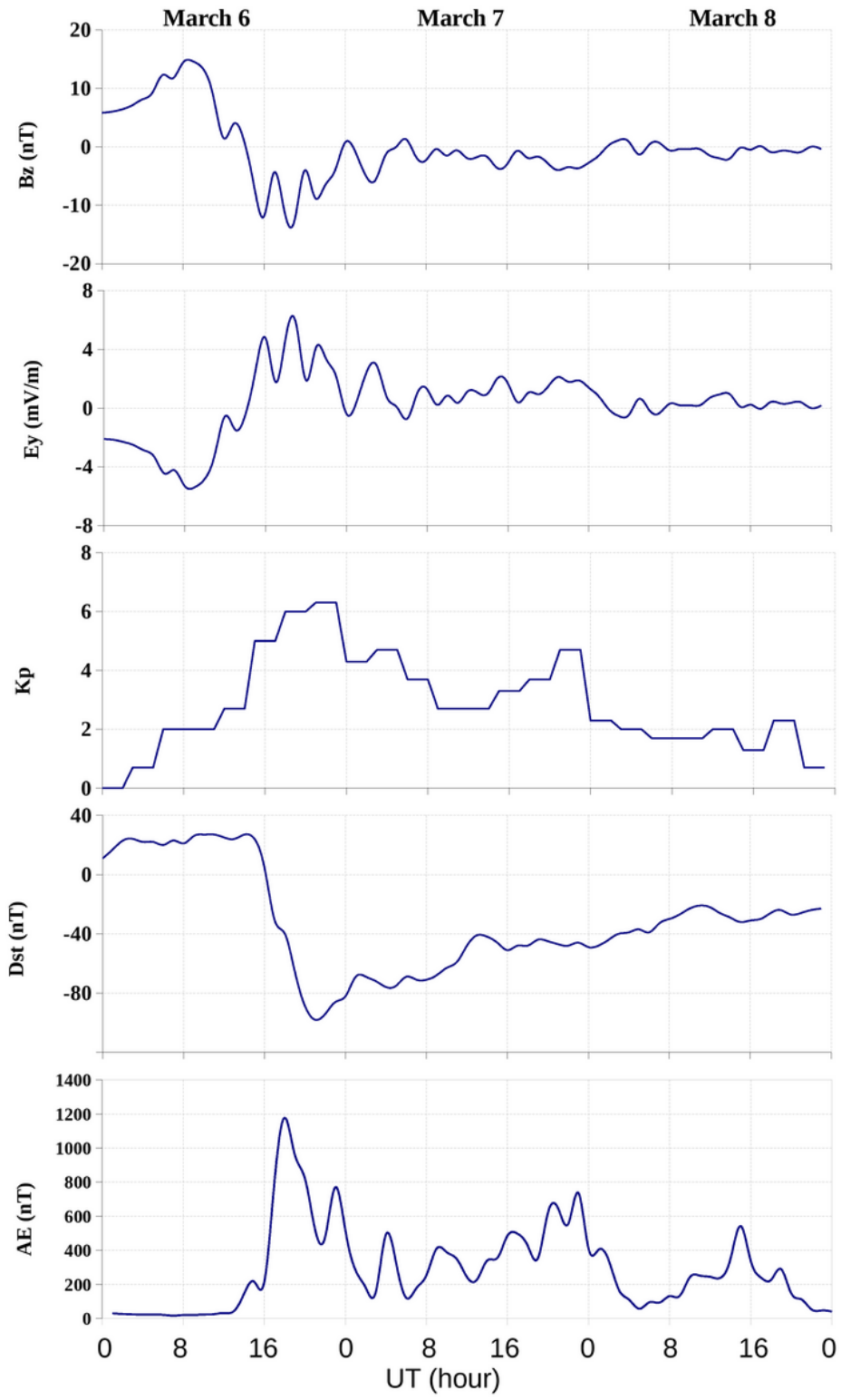

Figure 6

Bz, Ey, Kp, Dst and AE during 6-8 March 2016

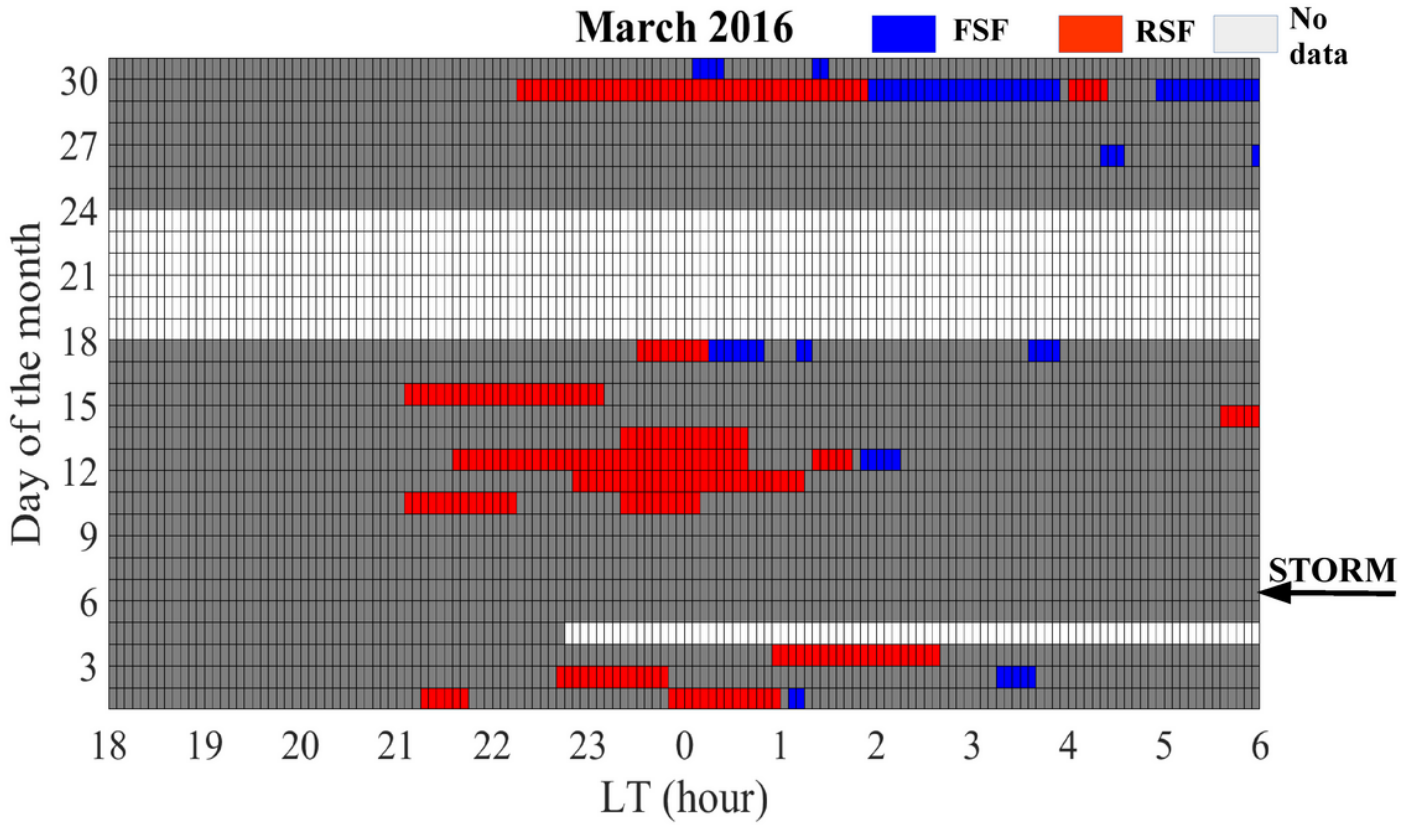

Figure 7

Range spread-F (RSF) occurrence (red) and frequency spread-F (FSF) occurrence (blue) at Tucumán during March 2016. White indicates data gaps

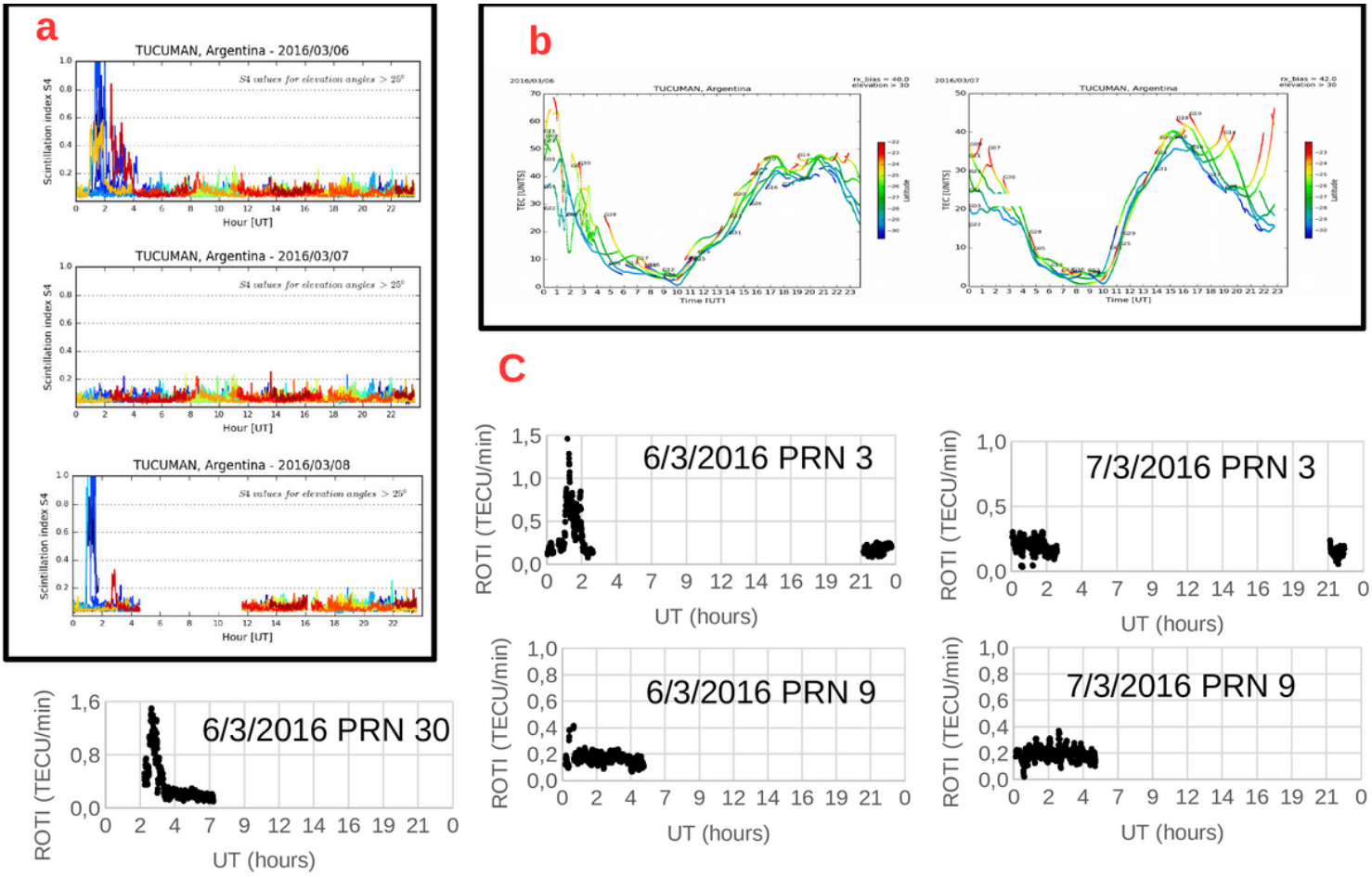

Figure 8

a) S4 index at Tucumán during 6-8 March 2016. Different colours indicate different satellites. b) TEC for different satellites at Tucumán during 6-7 March 2016 c) ROTI for PRN 3, 9 and 30 on 6 and 7 March 2016

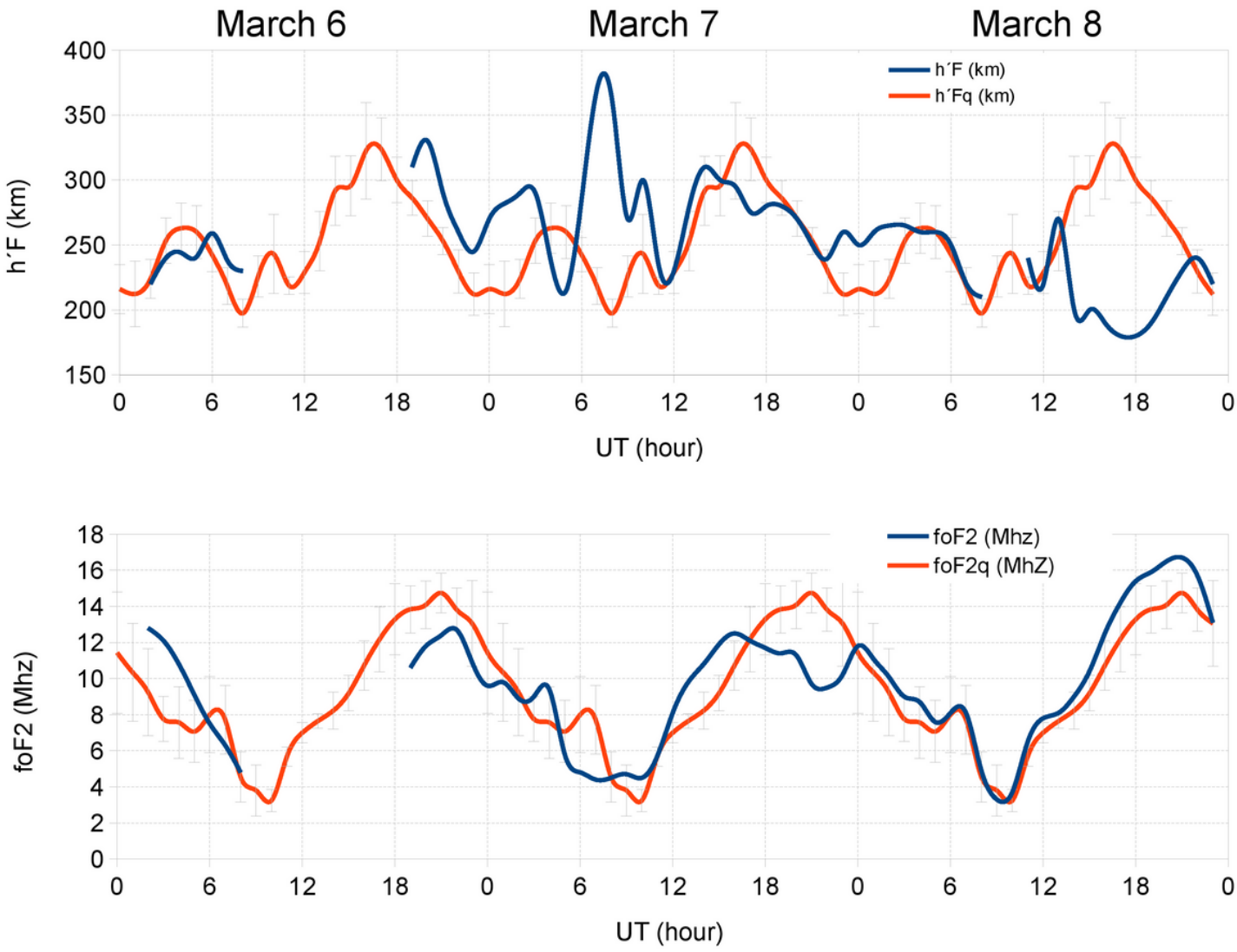

Figure 9

h´F (top) and foF2 (bottom) for Tucumán during 6-8 March 2016. The grey lines are ±1 standard deviation of the average quiet day's value

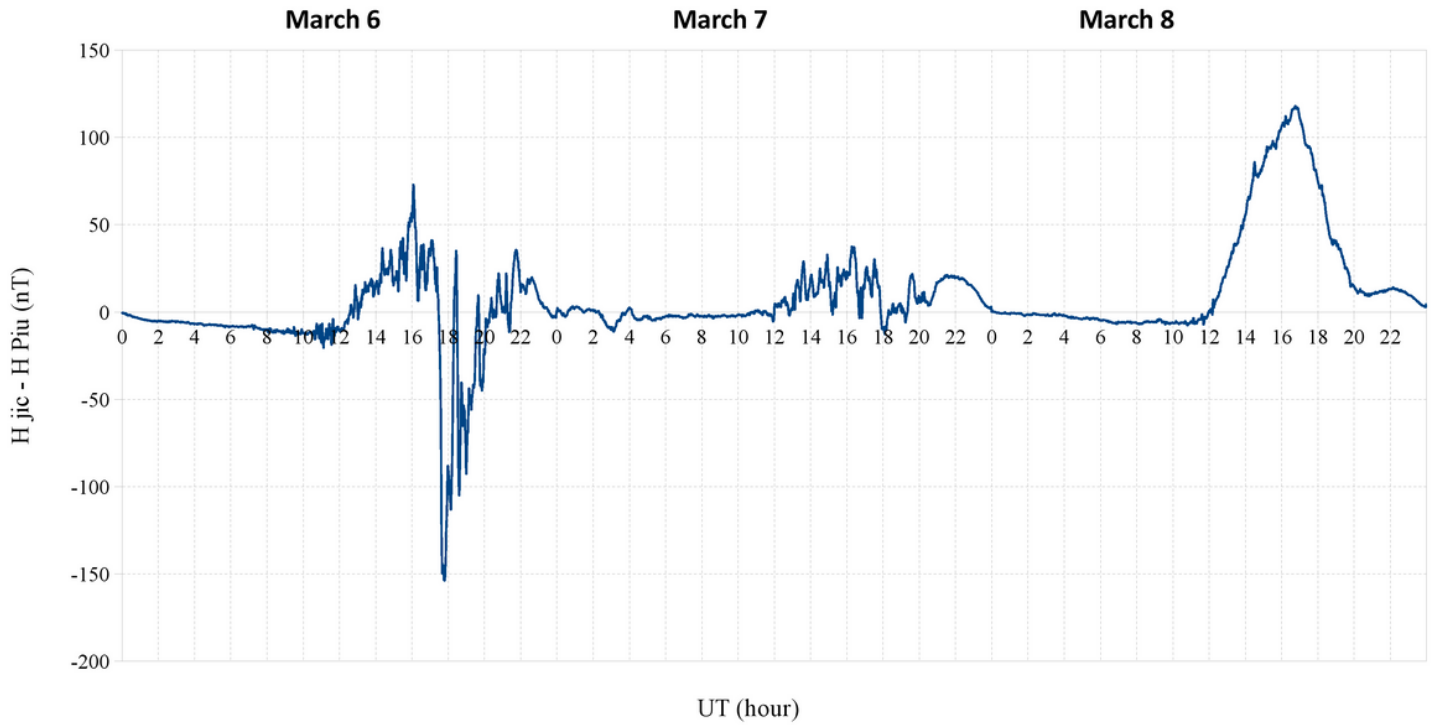

Figure 10

Difference between horizontal geomagnetic field components (H) at Jicamarca and Piura, Peru, during 6-8 March 2016

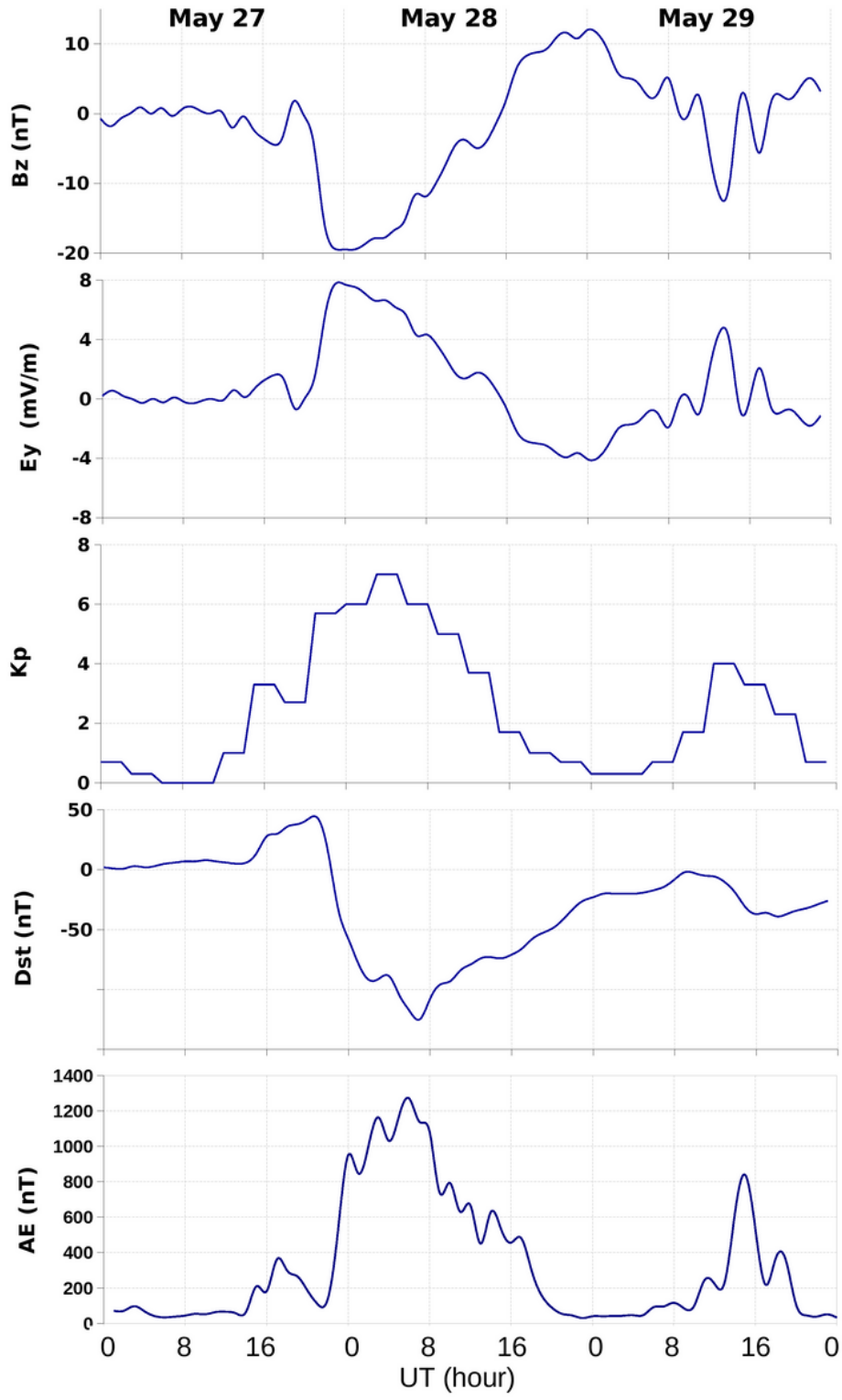

Figure 11

Bz, Ey, Kp, Dst and AE during 27-29 May 2017. The arrow indicates the sudden storm commencement (SSC)

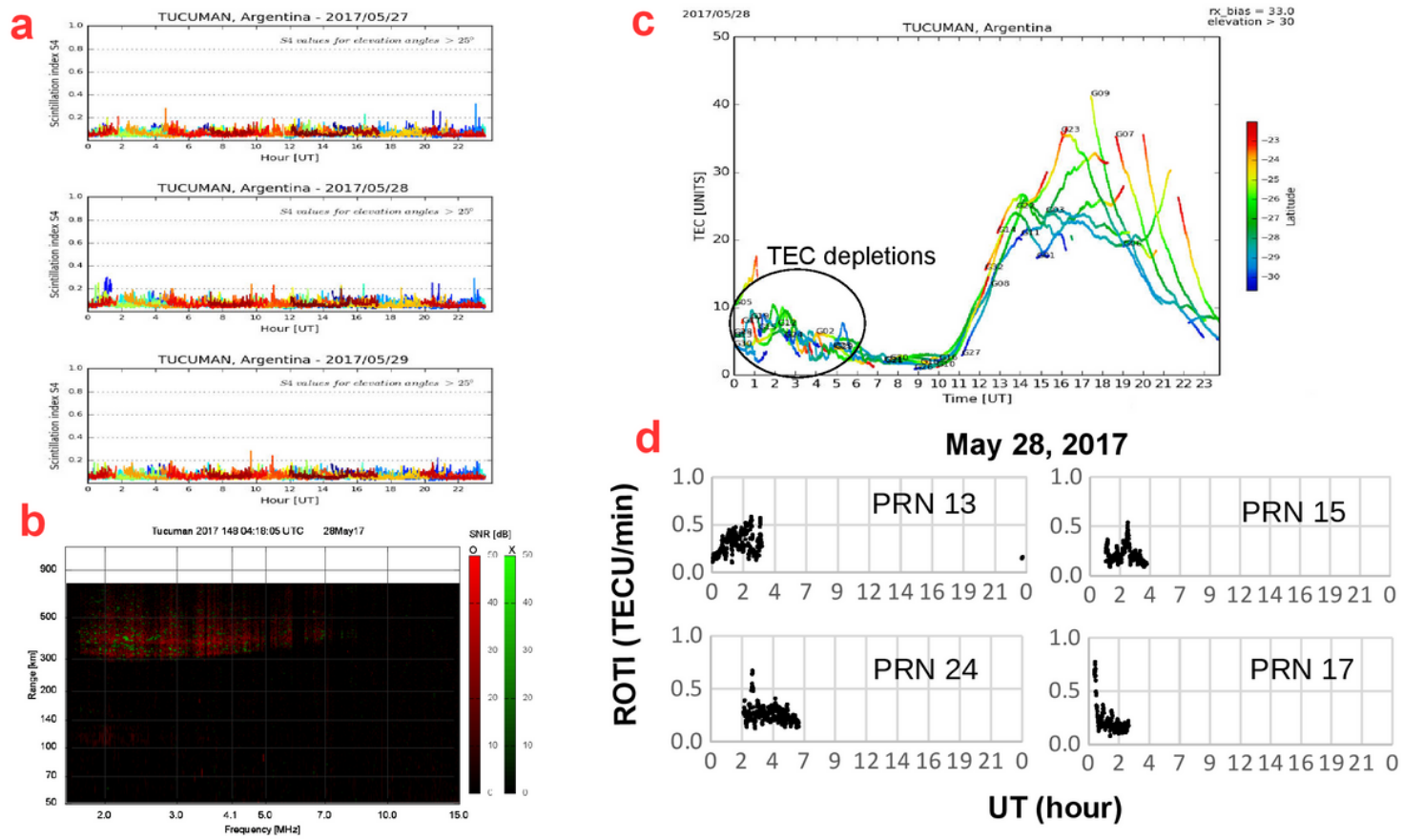

Figure 12

a) S4 index at Tucumán during 27-29 May 2017. Different colours indicate different satellites. b) Example of RSF observed in ionograms on 28 May 2017 at Tucumán c) TEC at Tucumán on 28 May. The circle indicates TEC depletion. d) ROTI for PRN 13, 15, 24 and 17 on 28 May 28 2017

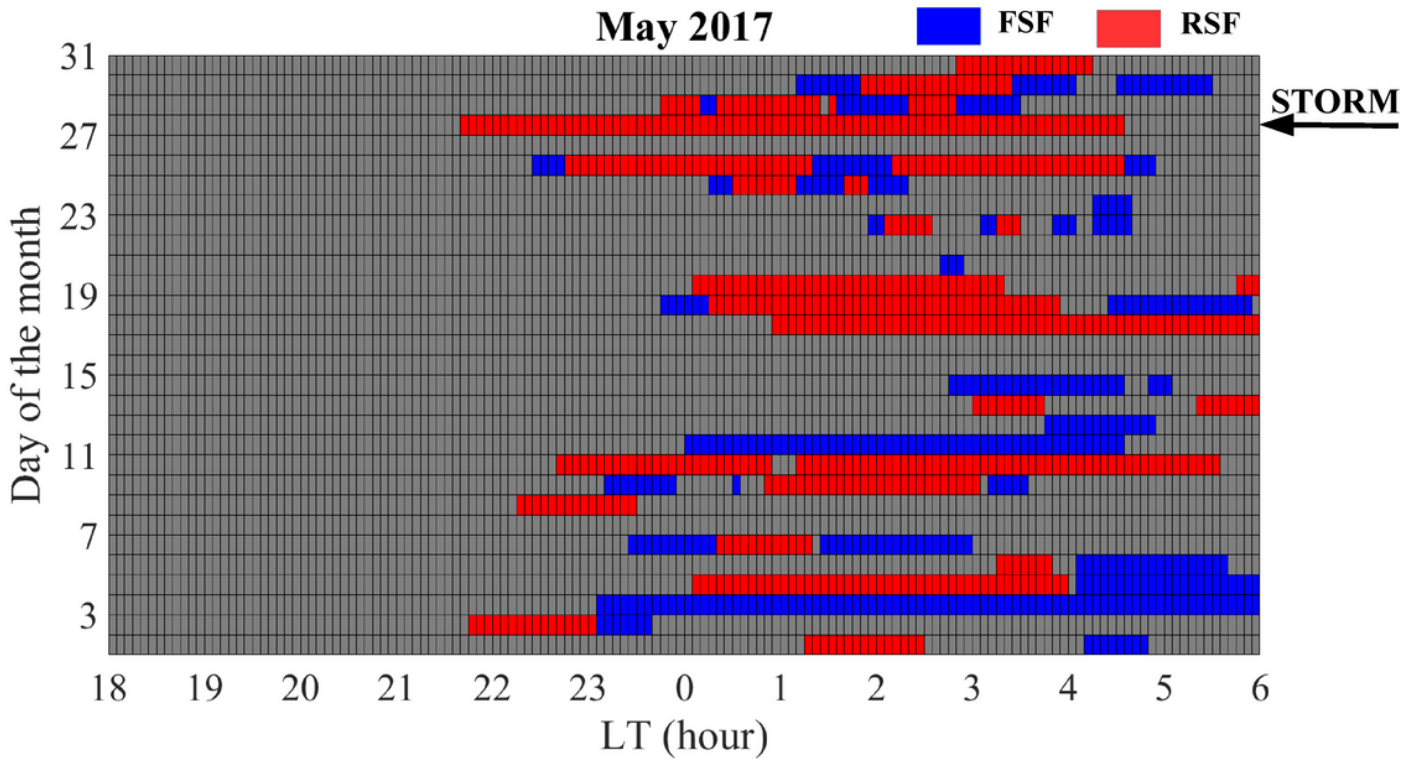

Figure 13

Range spread-F (RSF) occurrence (red) and frequency spread-F (FSF) occurrence (blue) at Tucumán during May 2017

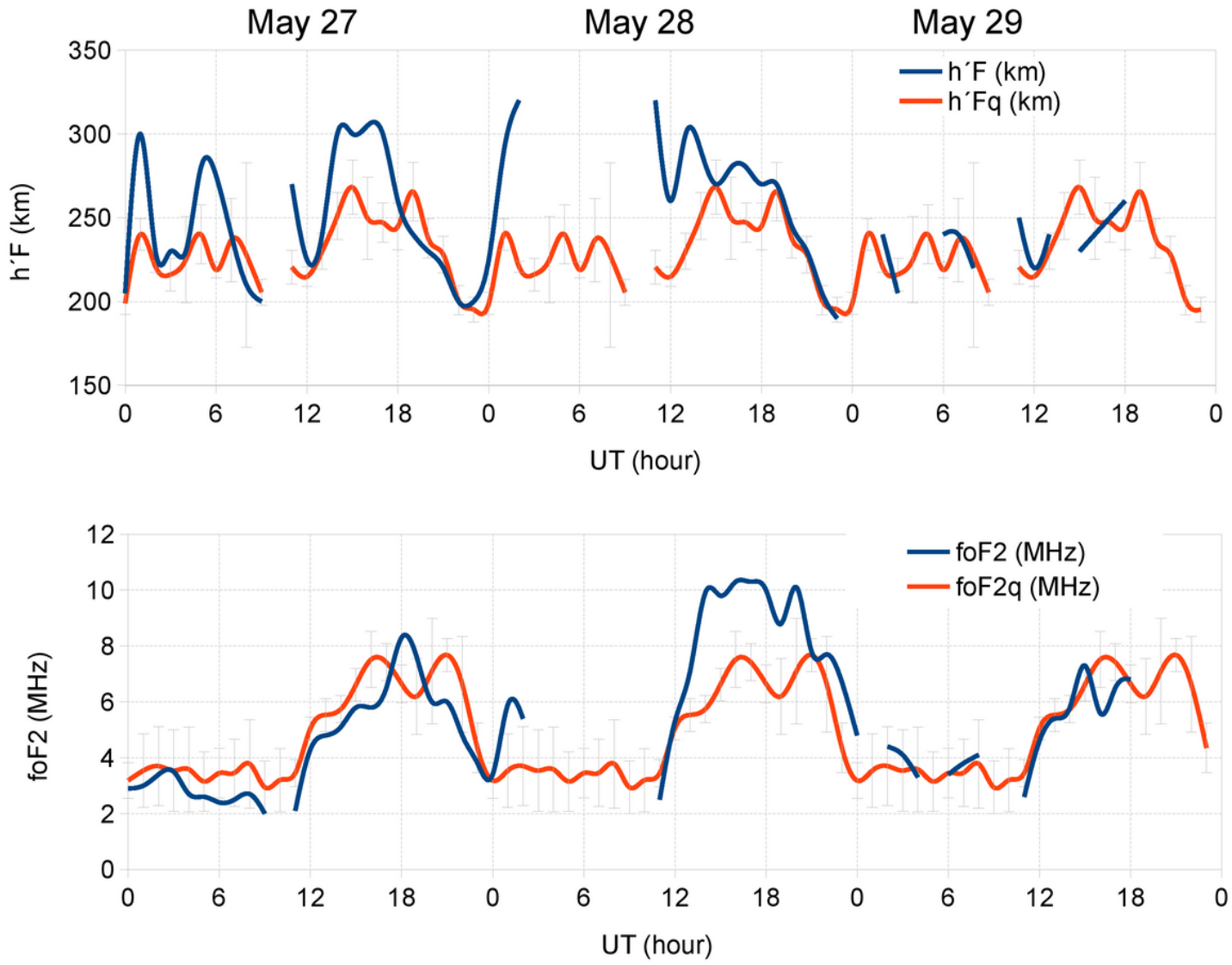

Figure 14

h´F (top) and foF2 (bottom) for Tucumán during 27-29 May 2017. The grey lines are ±1 standard deviation of the average quiet day's value

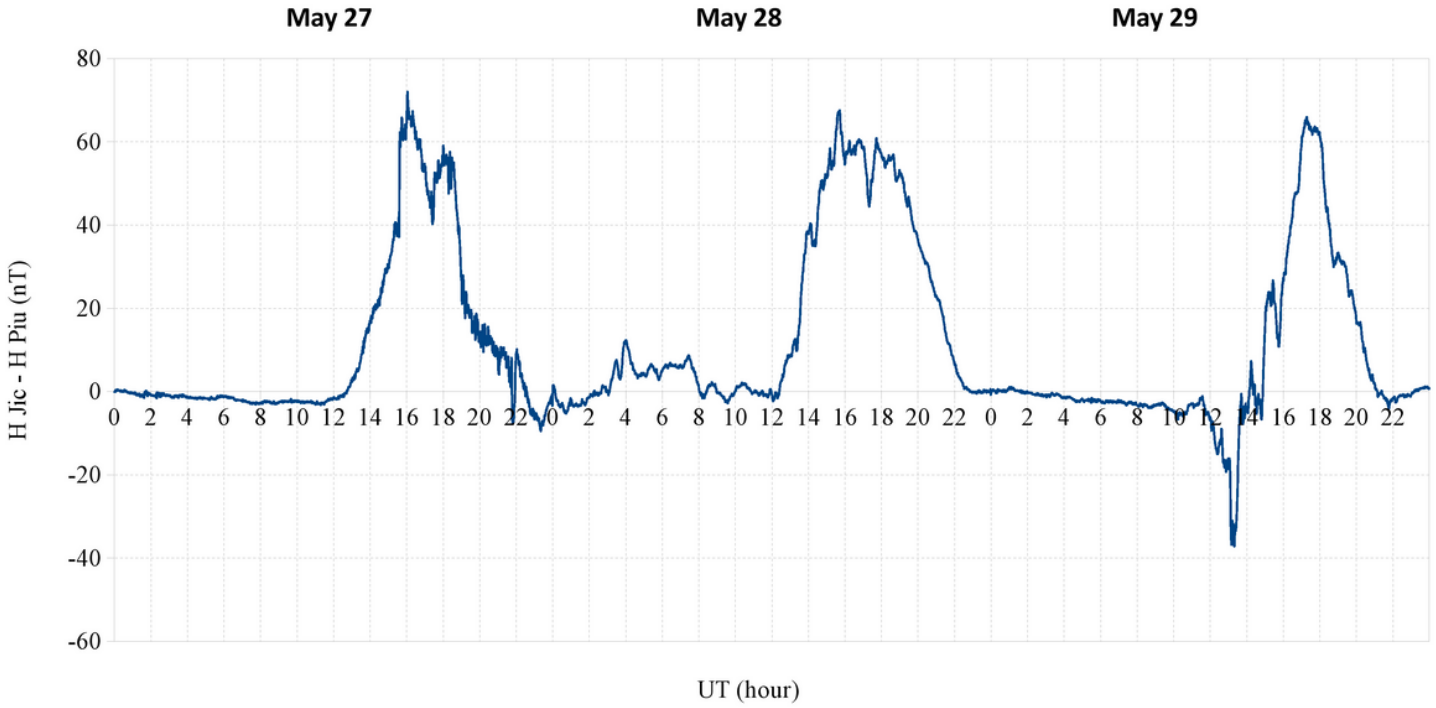

Figure 15

Difference between horizontal geomagnetic field components (H) at Jicamarca and Piura, Peru, during 27-29 May 2017

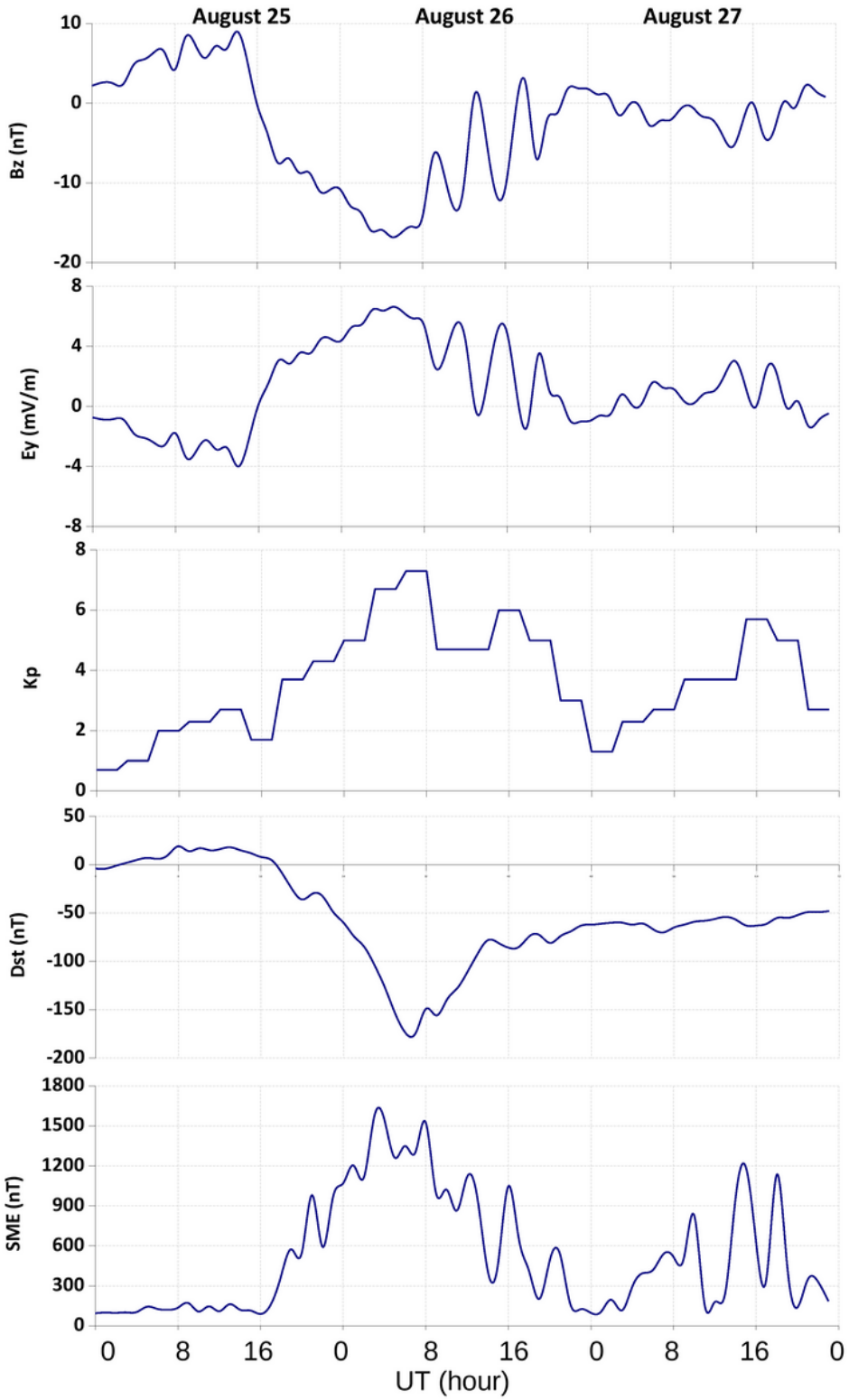

Figure 16

Bz, Ey, Kp, Dst and SME during 25-27 August 2018

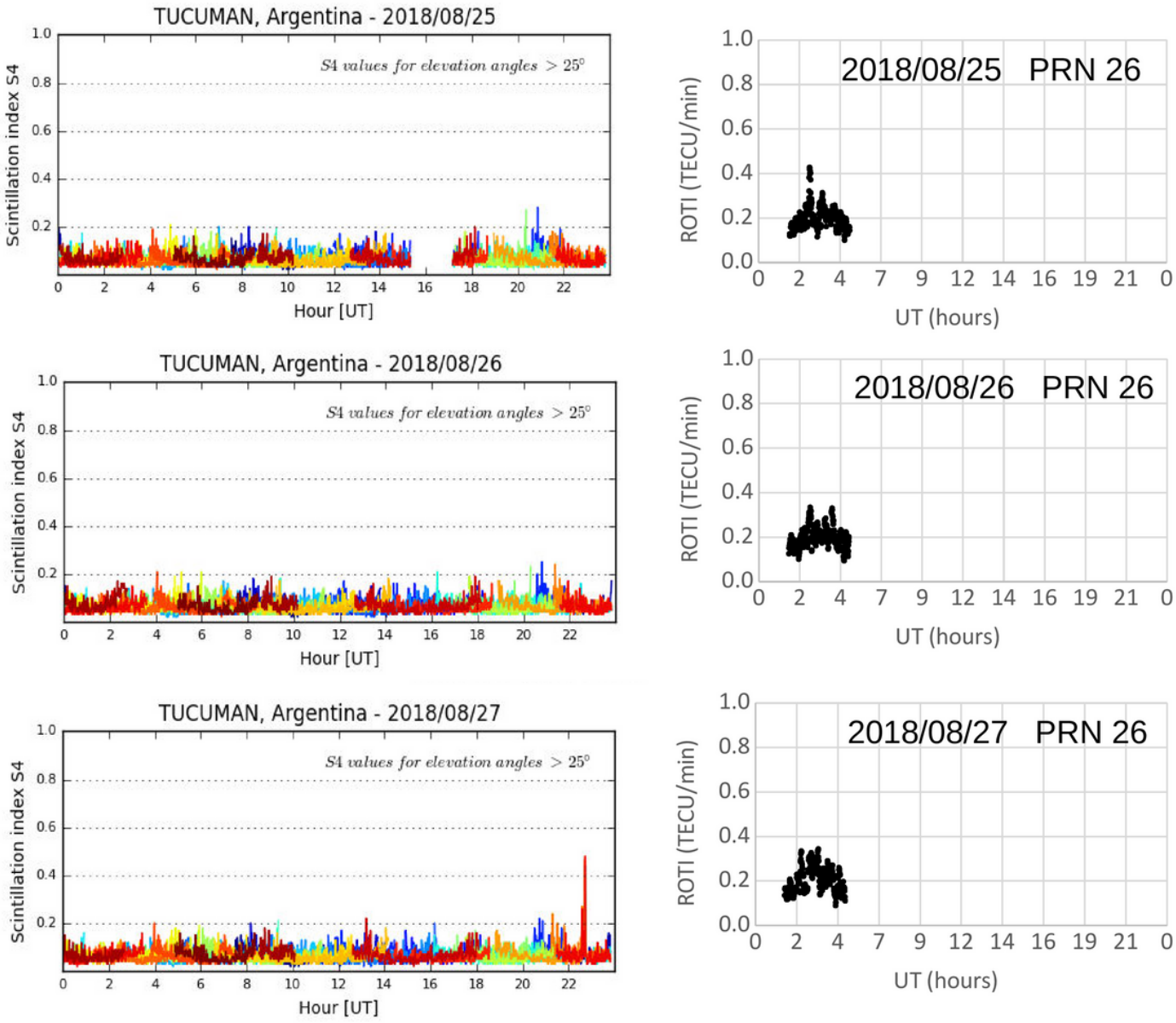

Figure 17

S4 index (left) at Tucumán during 25-27 August 2018. Different colours indicate different satellites. ROTI for PRN 26 (right) during 25-27 August 2018

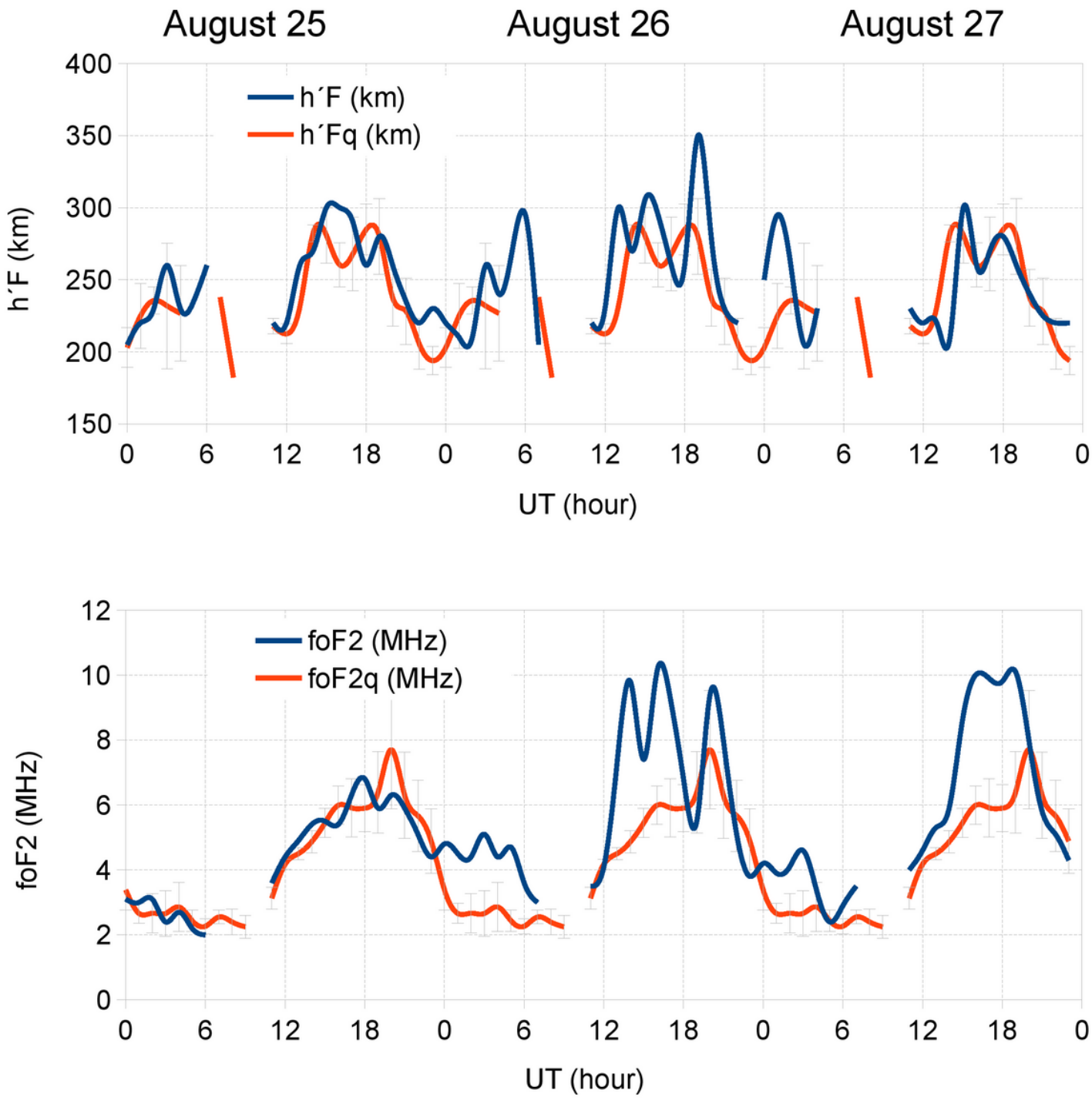

Figure 18

h´F (top) and foF2 (bottom) for Tucumán during 25-27 August 2018. The grey lines are ±1 standard deviation of the average quiet day's value

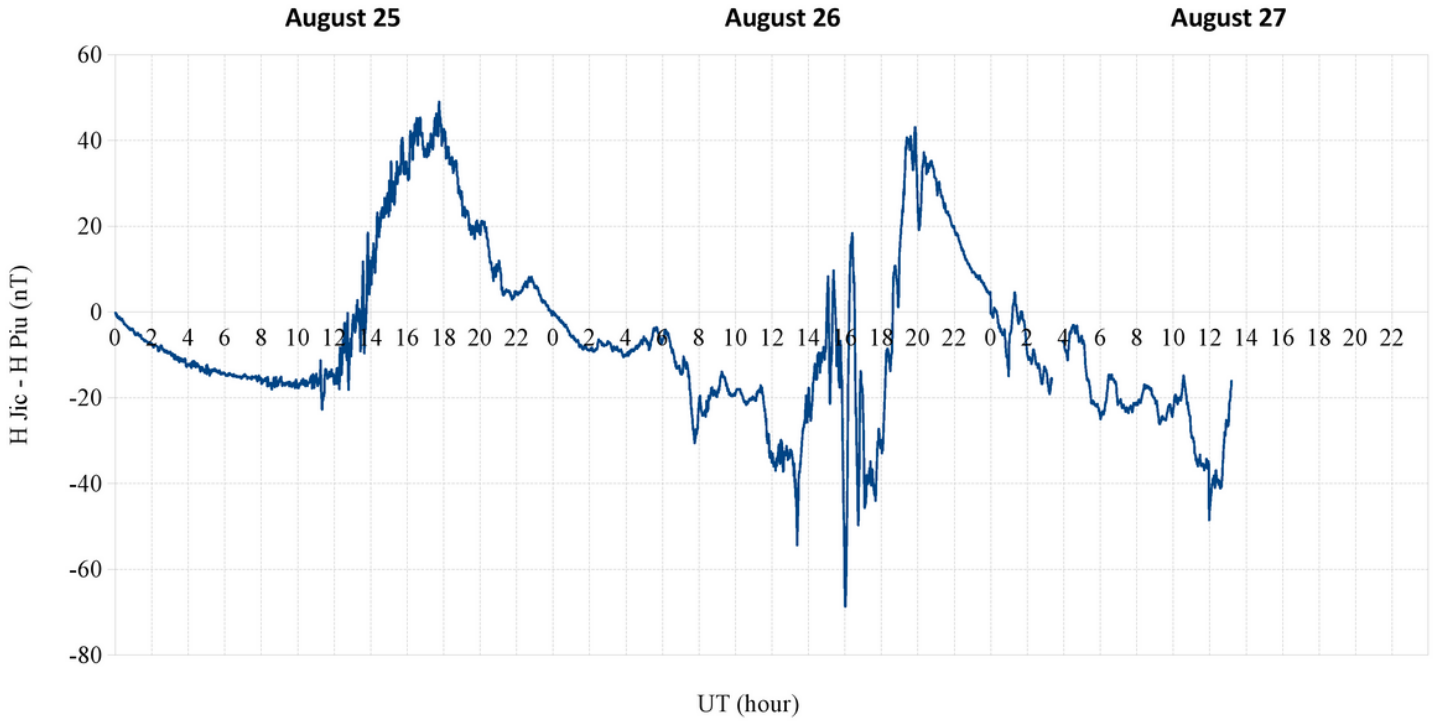

Figure 19

Difference between horizontal geomagnetic field components (H) at Jicamarca and Piura, Peru, during 25-27 August 2018